A selection and optimization strategy for single-domain antibodies targeting the PHF6 linear peptide within the Tau intrinsically disordered protein

Justine Mortelecque, O. Zejneli, S. Bégard, M. C. Simões, Lea El Hajjar, Marine Nguyen, Francois-Xavier Cantrelle, Xavier Hanoulle, J. C. Rain, Morvane Colin, et al.

JBC RESEARCH ARTICLE

A selection and optimization strategy for single-domain antibodies targeting the PHF6 linear peptide within the tau intrinsically disordered protein

Received for publication, July 19, 2023, and in revised form, February 15, 2024 Published, Papers in Press, March 12, 2024,
https://doi.org/10.1016/j.jbc.2024.107163

Justine Mortelecque[1,2], Orgeta Zejneli[1,2,3,‡], Séverine Bégard[3,‡], Margarida C. Simões[4,5], Lea ElHajjar[1,2], Marine Nguyen[1,2], François-Xavier Cantrelle[1,2], Xavier Hanoulle[1,2], Jean-Christophe Rain[6], Morvane Colin[3], Cláudio M. Gomes[4,5], Luc Buée[3,*], Isabelle Landrieu[1,2,*], Clément Danis[1,2,3], and Elian Dupré[1,2,*]

From the [1]CNRS EMR9002 – BSI - Integrative Structural Biology, Lille, France; [2]Univ. Lille, Inserm, CHU Lille, Institut Pasteur de Lille, U1167 - RID-AGE - Risk Factors and Molecular Determinants of Aging-Related Diseases, Lille, France; [3]Univ. Lille, Inserm, CHU-Lille, U1172 - LilNCog - Lille Neuroscience & Cognition, Lille, France; [4]BioISI - Instituto de Biosistemas e Ciências Integrativas, and [5]Departamento de Química e Bioquímica, Faculdade de Ciências, Universidade de Lisboa, Lisboa, Portugal; [6]Hybrigenic Services, Evry-Courcouronnes, France

Reviewed by members of the JBC Editorial Board. Edited by Roger Colbran

The use of variable domain of the heavy-chain of the heavy-chain-only antibodies (VHHs) as disease-modifying biomolecules in neurodegenerative disorders holds promises, including targeting of aggregation-sensitive proteins. Exploitation of their clinical values depends however on the capacity to deliver VHHs with optimal physico-chemical properties for their specific context of use. We described previously a VHH with high therapeutic potential in a family of neurodegenerative diseases called tauopathies. The activity of this promising parent VHH named Z70 relies on its binding within the central region of the tau protein. Accordingly, we carried out random mutagenesis followed by yeast two-hybrid screening to obtain optimized variants. The VHHs selected from this initial screen targeted the same epitope as VHH Z70 as shown using NMR spectroscopy and had indeed improved binding affinities according to dissociation constant values obtained by surface plasmon resonance spectroscopy. The improved affinities can be partially rationalized based on three-dimensional structures and NMR data of three complexes consisting of an optimized VHH and a peptide containing the tau epitope. Interestingly, the ability of the VHH variants to inhibit tau aggregation and seeding could not be predicted from their affinity alone. We indeed showed that the *in vitro* and *in cellulo* VHH stabilities are other limiting key factors to their efficacy. Our results demonstrate that only a complete pipeline of experiments, here described, permits a rational selection of optimized VHH variants, resulting in the selection of VHH variants with higher affinities and/or acting against tau seeding in cell models.

Variable heavy-chain of the heavy-chain–only antibodies (VHHs), also named single-domain antibodies or nanobodies (1), are the smallest domains of natural Camelidae single-chain antibodies that are still capable to recognize an antigen. Their many interesting properties and potential for engineering make VHHs ideal candidates for the design of innovative treatments (2) and new investigation tools (3, 4), including for in-cell imaging (5). Their clinical use has indeed been established in recent years, first with caplacizumab that targets von Willebrand factor to treat thrombotic thrombocytopenic purpura (6) and ozoralizumab that targets tumor-necrosis factor-alpha (and human serum albumin) to treat the chronic, autoimmune inflammatory disease rheumatoid arthritis (7). In this later case, the advantages stemming from the biochemical properties of VHHs were put forward, observed as a fast onset of action and the absence of secondary reaction, even in a model of prolonged treatment where no anti-VHH antibodies were formed (8). VHH development covers many additional applications and is gaining ground in neurodegenerative disorders (9, 10) although their medical use in this field has not yet been demonstrated. However, given their better potential than immunoglobulins to be delivered to the central nervous system (11), they are considered as biomolecules of high interest to be developed as disease-modifying next-generation treatments for related pathologies.

VHHs targeting a specific epitope can be generated either through animal immunization (generally in llamas) and screening of the immunized library (12) or directly through the screening of a naïve synthetic library without animal handling (13). VHHs rarely target intrinsically disordered proteins and peptides (14, 15). Nevertheless, VHHs that target the prion protein, alpha-synuclein protein, Aβ (amyloid) peptides, and tau protein (16–20), which are all involved in neurodegeneration linked to aggregation, have been reported and shown to block their self-assembly process (21) either *in vitro* or in the cytoplasmic compartment of cells (22).

Tauopathies, including Alzheimer's disease, are neurodegenerative diseases characterized by the accumulation of tau proteins inside neurons that form well-organized fibrillary aggregates named paired helical filaments (PHF) that may

‡ These authors contributed equally to this work.
* For correspondence: Dr Isabelle Landrieu, isabelle.landrieu@univ-lille.fr; Dr Luc Buée, luc.buee@inserm.fr; Dr Elian Dupré, elian.dupre@univ-lille.fr.

disrupt the normal neuronal functions (23). Structures of these PHFs have been resolved with atomic detail, showing a typical amyloid beta fold of cross-beta sheet arrangement along the fiber axis (24, 25). These diseases are defined by a specific spatial and chronological evolution that is now recognized to be linked to a seeding and stereotypical propagation process in which a pathological tau, a poorly defined species, will be transferred along neuronal networks and template soluble tau to nucleate fiber formation (26–28). Importantly, the clinical symptoms correlate with tau deposition in the brain regions (29, 30), indicating that decreasing tau filament formation and propagation through the brain is important to slow down tauopathy evolution. The potential to use VHHs to achieve this goal needs to be evaluated.

VHHs have indeed many interesting biophysico-chemical properties stemming from their low size and unique chain. They present several advantages such as an easy recombinant production in different systems be it prokaryotes, yeasts, or insect cells and more (31), good stability and engineering properties (15). This leads to many opportunities to optimize those VHHs for specific use, considering their production (32), their affinity (33), their stability (34), or their capacity of being produced intracellularly (9, 16, 35). In relation to this last point, a significant part of VHHs may be unable to fold properly in the reducing environment of the cytoplasm (4, 36), which inhibits the formation of the disulfide bridges that contribute to the VHH stability, leading to aggregation or degradation (35, 37). Improving intracellular stability and solubility of the VHHs thus requires specific engineering approaches or selection. Indeed, many efforts to engineer intrabody stability or solubility were already invested for VHHs and other types of single-domain antibodies through molecular evolution (38), random or targeted amino-acid replacement (39, 40), or as protein fusions (41, 42). These various processes to engineer the VHH physico-chemical properties for specific uses remain highly empirical and pipelines to reach improved properties still need to be better defined.

Given the progress made in the clinical use of VHHs and their interest in neurodegenerative proteinopathies, VHHs have been selected against the neuronal tau protein to develop new research tools and evaluate their therapeutic potential (16, 20). We initially focused on VHH E4-1 that has the capacity to block *in vitro* tau aggregation but not tau aggregation seeding in a cell-reporter model (16). Cell assays show that VHH E4-1 is indeed not stable when expressed in eukaryotic cells. The interest in blocking tau aggregation in neurons, in a subset of neurodegenerative diseases commonly referred to as tauopathies, including the most prevalent Alzheimer's disease, led to the optimization of VHH E4-1 for intracellular use, resulting in the selection of VHH Z70. This VHH is able to block tau aggregation seeding in a reporter cell line and in a ThyTau transgenic murine model of tauopathies (16). Given these promising results showing that VHH Z70 can be used to block tau aggregation inside neurons and the potential of VHHs to reach nanomolar affinities, further optimization was considered.

We therefore developed an optimization strategy to increase the ability of the lead VHH Z70 to bind its tau target in the cellular environment. This optimization was challenging given the already high affinity of VHH Z70 for tau and without compromising binding specificity and other important properties, including conformational stability in cell for intracellular applications. We set up a pipeline of experiments that all seem important to evaluate the properties of VHHs and succeeded in selecting variant VHHs that retained the optimal properties depending on the context of their use. Some VHHs (mutants 1, 3, and 20), thanks to their increased affinity for tau protein, would work well as recombinant proteins delivered to the cells, while a subset (mutants 1 and 3) showed their efficiency in blocking tau seeding when directly expressed in cells.

Results

Affinity optimization of VHH Z70

To generate optimized variants of VHH Z70 (hereafter Z70), a strategy of limited random mutagenesis coupled with stringent selection by yeast two-hybrid screening was chosen for binding optimization in intracellular conditions. A complementary deoxyribonucleic acid mutant library was thus first built by random mutagenesis, targeting the whole sequence of Z70 to produce a variety of VHH preys (N-terminal GAL4-activation domain fusion, GAL4ADZ70) against the tau bait (C-terminal LexA fusion, Tau-LexA). The library was transformed in yeast, and screening of the library was carried out by cell-to-cell mating on selective medium. The interaction between the bait (Tau-LexA) and prey (GAL4ADZ70) was detected by the growth of a diploid yeast colony on the selective medium. Growth of this colony, auxotrophic for histidine, is dependent on the transcription of the his3 reporter gene, which requires interaction between the bait and the prey. Mutants of Z70 with an improved affinity for tau were selected on medium without histidine (His-) by increasing the selection pressure using 3-amino-1,2,4-triazole (3AT), with the latter compound being a competitive inhibitor of the his3 reporter gene product, to reach conditions with limited to undetected interaction of Z70 with tau (100 mM 3AT). Forty-three mutants were thus obtained and their sequence analyzed (Fig. S1).

VHH Z70 mutants' sequences selection

Mutants contained 1 to 4 different point mutations resulting in amino acid substitutions and 33 different amino acid positions were found substituted at least once (Fig. 1*A*). Most substitutions occurred in the framework, with only one position in complementarity-defining region 1 (CDR1) (T32), three in CDR2 (E56, G58, S59), and 1 in CDR3 (P101). Interestingly, three positions were highly represented, G115 (23.6% of occurrences, 21 occurrences, always substituted with glutamic acid), R47 (15.7%), and S23 (9%), whereas the others were randomly found between one and four times (<5%). Among these three positions, S23 was never found mutated alone but mostly in combination with G115. Conversely, G115 and R47 mutations were never found in combination.

A

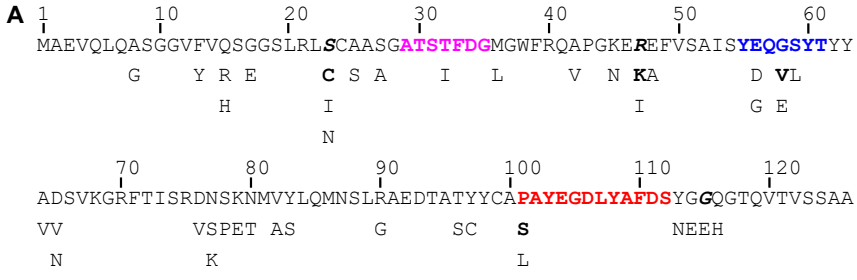

B

VHH	Substitutions	Domain
Mut 1	G115E	FR4
Mut 3	R47K	FR2
Mut 5	T96S	FR3
Mut 9	P101S + G115E	CDR3 + FR4
Mut 12	S23C + G115E	FR1 + FR4
Mut 14	T32I + E56G + G115E	CDR1 + CDR2 + FR4
Mut 15	R90G + P101S + G114E	FR3 + CDR3 + FR4
Mut 20	R47K + G115E	FR2 + FR4

Figure 1. Selected mutations for VHH optimization. *A*, sequence of VHH Z70 and selected substitutions. CDR1, 2, and 3 sequences are represented in *pink*, *blue*, and *red* respectively. The three amino acids in *bold italic* are the most frequently substituted. When different substitutions exist that differ in frequency, the most frequent is in *bold*. *B*, overview of the mutants selected for further analysis. CDR, complementarity-defining region; VHH, variable heavy-chain of the heavy-chain–only antibody.

Z70 was already an optimized variant of lead VHH E4-1 as previously described (16), and among the mutations that lead to Z70 only W114G in the framework region (FR4) was found further mutated to glutamic acid in this screen (one occurrence: mutant 15, G114E in combination with mutations R90G and P101S).

We chose a subset of seven Z70 mutants to represent the variety of mutations, ranging from single to triple mutations and covering FRs and CDRs (Fig. 1*B*). These selected VHHs had comparable or better interaction with tau 0N4R than Z70 in yeast two-hybrid system according to one-to-one mating assays (Fig. S2). We generated a last mutant, called mutant 20, containing the two most prominent mutations G115E and R47K that were not found in combination during the initial screen.

Affinity measurement

Selection of the optimized mutants was based on their apparent better affinity in a yeast two-hybrid assay compared to Z70. We used surface plasmon resonance (SPR) spectroscopy to confirm and quantify the improved affinities of those mutants using recombinant proteins. Biotinylated tau 2N4R was immobilized on a streptavidin (SA) chip, and the different VHHs were tested as analytes in single-cycle kinetics that consist in increasing the analyte concentration in successive passages, without dissociation or regeneration. All eight mutants indeed showed a better affinity than Z70 toward full-length tau in this assay, further validating the selection process (Table 1, Fig. S3). Interestingly, the kinetics of the interaction varied depending on the mutant. In most mutants, both k_{on} and k_{off} values were decreased and increased, respectively, except for mutant 5 (T96S) and mutant 15 (R90G + P101S + G114E), which had only either their k_{off} or k_{on} improved, respectively. Substitution G115E (mutant 1), which was the most frequent in the initial set of mutants, improved drastically the k_{on} by itself, leading to the best overall affinity (23 nM) measured in this screen. This increased affinity was still observed when combined with additional substitutions in other mutants (mutants 9, 12, 14 and 20), but not improved. The k_{off}, which might be an interesting parameter as it relates to the time of residence of the VHH on the tau protein, showed the best improvement for mutants 5 and 20 (R47K + G115E).

Epitope verification

While most amino acid substitutions occurring in the FRs of the mutants were not expected to modify the Z70 epitope, the optimization screen was carried out to select better binders with full-length tau bait and modification of the recognition site could thus not be completely ruled out. We first checked whether the VHHs still directly detect tau using a fluorophore-conjugated VHH. We labeled Z70, mutants 1 (G115E), 3 (R47K), and 20 (double mutation) with carboxytetramethylrhodamine and used them as probes in Western blots for direct visualization. They were all able to recognize tau in this setup and their sensitivity did not show drastic changes compared to Z70 (Fig. 2*A*).

Table 1

Interaction kinetics between the different VHH and full-length tau measured by SPR

VHH	ka(1/M.s)*10^{+2}	kd(1/s)*10^{-5}	Kd(nM)
Z70	181 ± 0.42	267 ± 1.5	147.8 ± 0.9
Mut1	**1070 ± 17**	242 ± 3.05	**22.7 ± 0.5**
Mut3	260 ± 3.5	210 ± 2.8	80.5 ± 1.5
Mut5	109 ± 0.32	**88.2 ± 1.6**	80.8 ± 1.5
Mut9	401 ± 1.5	205 ± 2.4	51.1 ± 0.6
Mut12	339 ± 2.4	207 ± 1.2	61.2 ± 0.6
Mut14	188 ± 0.46	140 ± 1.6	74.3 ± 0.8
Mut15	653 ± 7.1	277 ± 3.2	42.5 ± 0.7
Mut20	213 ± 1.8	**89.0 ± 1.3**	41.8 ± 0.7

SPR, surface plasmon resonance; VHH, variable heavy-chain of the heavy-chain–only antibody.
The highest value of ka and lowest values of kd and Kd are in bold characters.

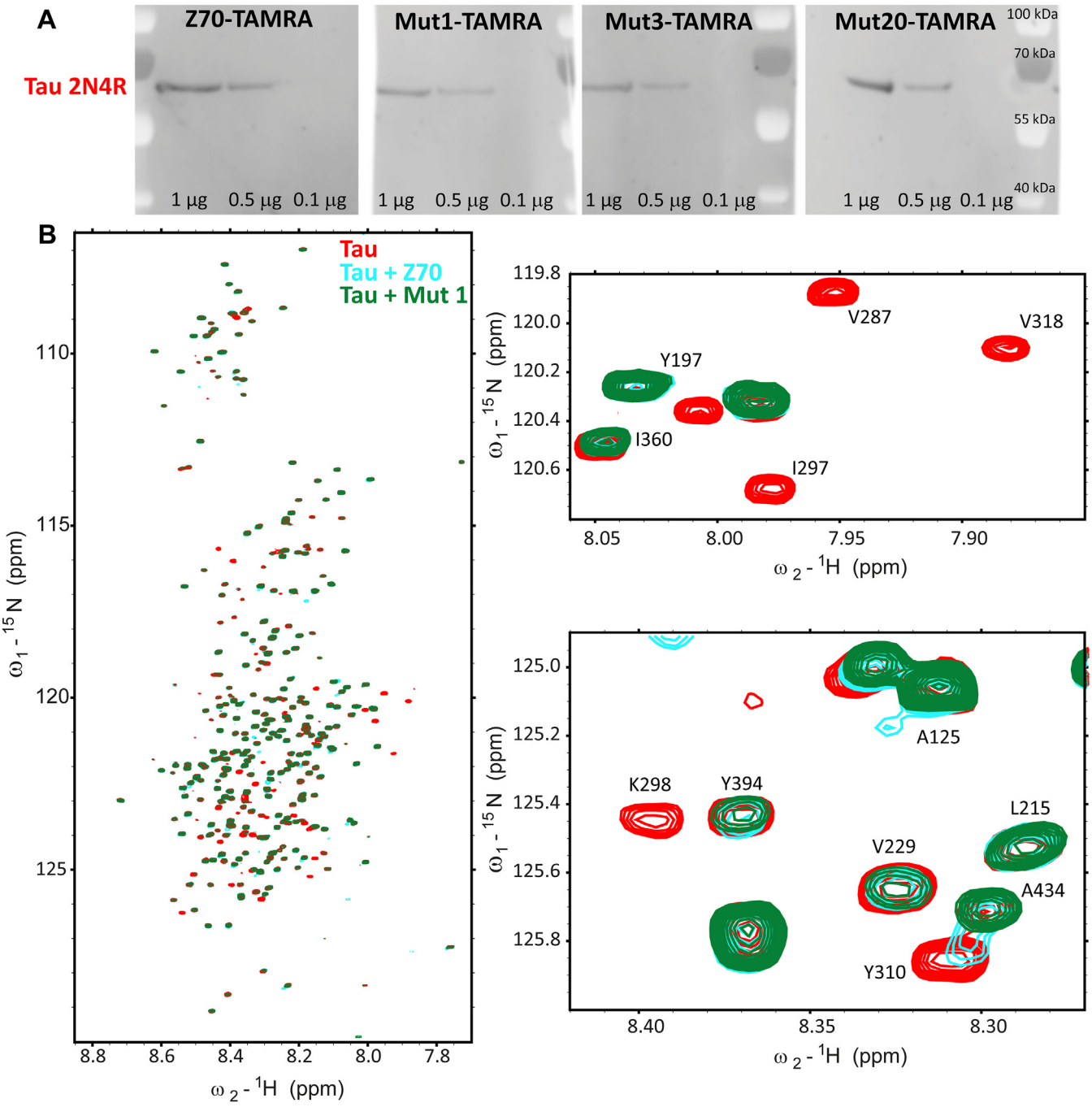

Figure 2. Epitope verification of Z70 mutants. *A*, Western blot against tau using TAMRA-labeled VHHs. *B*, spectrum overlay of tau alone (in *red*), tau with Z70 (in *blue*, 1:1 M ratio), or tau with mutant 1 (in *cyan*, 1:1 M ratio). TAMRA, carboxytetramethylrhodamine; VHH, variable heavy-chain of the heavy-chain–only antibody.

To obtain further molecular detail on the interaction of the eight different mutant VHHs, we used ^{1}H,^{15}N resonance intensity in 2D NMR spectra of tau as reporters at each amino acid position in tau sequence (Figs. 2*B*, 3 and S4). The intensity profile is well conserved between the different VHHs with a major loss of intensity for resonances corresponding to residues located in the R3 repeat, similarly to the reported effect of Z70 binding to tau PHF6 motif (Fig. 3) (16). As previously reported for Z70, secondary sites of interaction were observed, at the C terminus of the tau proline-rich domain and in the R2 repeat, as monitored by the loss of intensity of the corresponding resonances in the spectra of tau upon interaction (Figs. 3 and S4). Superposition of the tau spectra obtained for each VHH revealed subtle differences that might be due to differences in the kinetics of the interaction between tau and the VHHs because resonance intensity is not strictly related to binding but also to local dynamics and kinetics of the interaction (43) (Table 1). Even for mutant 9, which has the P101S mutation within the CDR3 recognition loop, the perturbations of the resonances were similar to those observed upon Z70

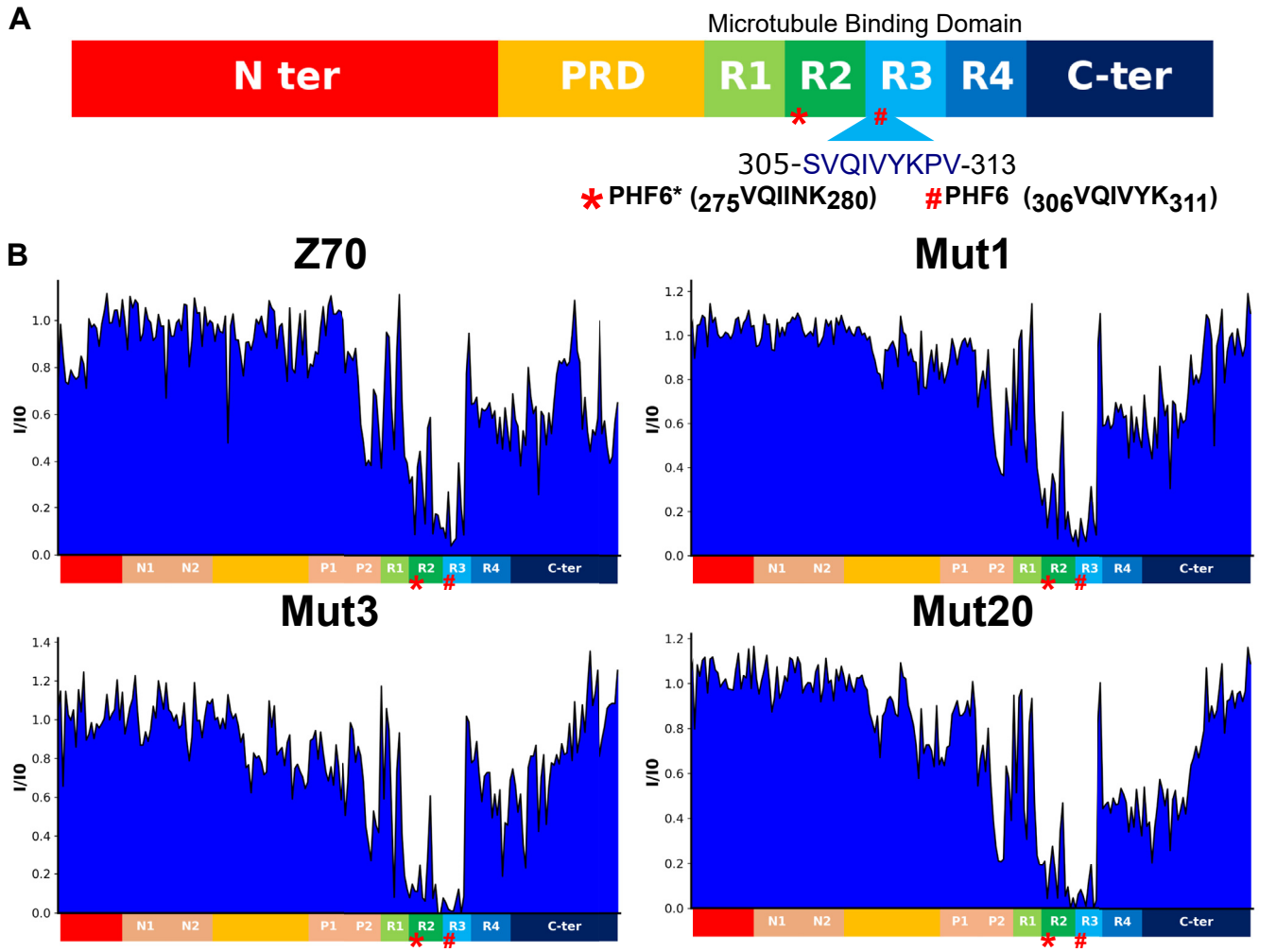

Figure 3. Epitope of Z70 and variant VHHs. *A*, schematic representation of the tau protein. N-terminal domain (1–163) is represented in *red* and may contain N1 and N2 inserted sequences depending on tau isoforms. The proline-rich domain (PRD) is subdivided in P1 and P2 regions. The microtubule binding domain consists of four partially repeated regions, R1 to R4 (in tau 4R). The R2 repeat is not present in tau 3R. C-ter is for the C-terminal domain. *B*, normalized intensity ratios I/I0 of corresponding resonances in the two-dimensional spectra of tau with equimolar quantity of Z70, mutant 1, 3, or 20 (I) or free in solution (I0) for residues along the tau sequence.

binding to tau, confirming the conservation of the PHF6 motif inside R3 as the main interaction site of the whole series of VHHs. For mutant 15 (triple mutation), which also contains the P101S mutation within the CDR3, addition to tau led to extended loss of intensity for many tau resonances. This was attributed to the formation of aggregates in the conditions of this assay that prevented definitive confirmation of the conservation of the Z70 epitope.

Effect of substitutions on the structure of mutant VHHs in complex with their peptide epitope

To rationalize the potential effect of the mutations on the interaction, and particularly the effect of the most abundant mutations in the screen, G115E and R47K, we have solved the structures of mutants 1 (G115E), 3 (R47K), and 20 (G115E + R47K) in complex with a tau[301-312] peptide by X-ray crystallography. We previously reported the crystallographic structure of Z70 in complex with the same peptide containing the PHF6 motif (16) (Protein Data Bank [PDB] code: 7QCQ), allowing a straightforward comparison. The structures obtained at a resolution of 1.83 Å, 2.35 Å, and 1.54 Å for mutant 1, 3, and 20, respectively, showed no major conformational differences with the parent Z70 bound to its epitope with backbone RMSD values of 0.517 Å between mutant 1 and Z70, 0.545 Å between mutant 3 and Z70, and 0.455 Å between mutant 20 and Z70. (Fig. 4). The interaction between these VHHs and the PHF6 tau peptide were conserved and involved the formation of a short intermolecular β-sheet between the VHH CDR3 and the PHF6 peptide as previously described for Z70 in (16) (Fig. 5*A*). G115 in Z70 is in a flexible loop (from F110 to G117) that is partially not resolved in the structure (from D111 to G115), whereas E115 electron density in mutant 20 was well defined. Conversely, three residues of this loop (S112-Y113-G114) remained unresolved in the absence of an electron density. Similarly, in mutant 1, this loop remained partially unresolved but some partial electron density can be observed for E115, even if not sufficient to permit a residue replacement. Mutant 3 did not show any more electron density than Z70 for G115, illustrating the importance of the E115

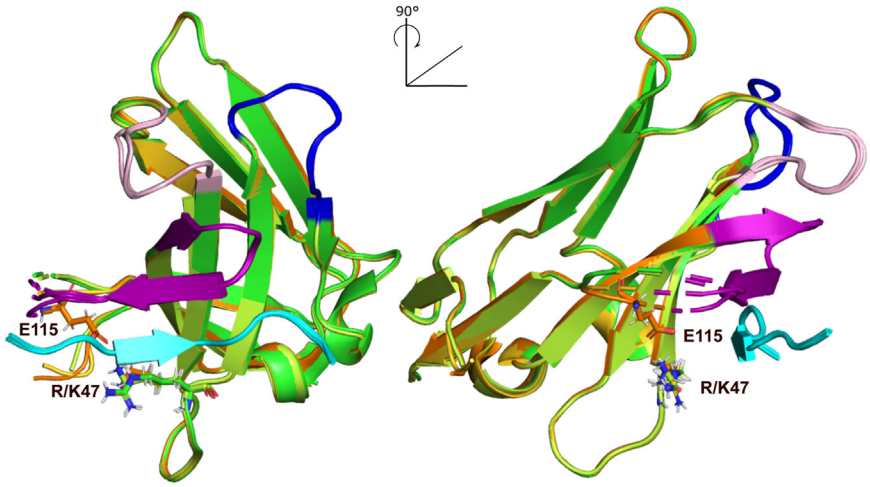

Figure 4. Comparison of Z70, mutant 1, 3, and 20 structures. Superposition of Z70 (in *green*, PDB 7qcq), mutant 1 (in *gold*, PDB 8opi), mutant 3 (in *pale green*, PDB 8pii), and mutant 20 (in *orange*, PDB 8op0). Their CDR1 are in *pink*, CDR2 in *blue*, and CDR3 in *purple*. Tau PHF6 peptide is colored *cyan*. CDR, complementarity-defining region; PDB, Protein Data Bank.

substitution in tightening this loop (Fig. 5*B*). G115 in Z70 or mutant 3 and E115 in mutant 1 were thus not modeled in the structures due to the high flexibility of this loop region (Fig. 4). Reversely, positioning of the side chains of residues E115 and K47 in close proximity in mutant 20 suggested the formation of a salt bridge that could tether part of the CDR3 long loop to the core of the VHH (Fig. 6*A*).

In view of the very high similarity of all the structures, including for the residues in direct interaction with the bound peptide, we hypothesized that modification of the conformational dynamics of the VHHs could contribute to the affinity increase (44, 45). We thus next used NMR spectroscopy of the VHHs to go beyond the static view as the linewidth of the $^{1}H,^{15}N$ resonances reports on these internal dynamics, observed as an exchange broadening of the resonances affecting the peak intensities. The $^{1}H,^{15}N$ spectra of all the VHHs indeed hinted at conformational dynamics because of their poor quality, as seen by the small number of detected resonances due to line broadening (Figs. 6*B* and S5). Confirmation that the line broadening can indeed be assigned to conformational exchange came from the spectra of the peptide-bound VHHs, as in this case, additional resonances were detected suggesting stabilization of preferential conformational state(s) (Fig. S6). Compared to Z70, mutant 20 showed an improved spectrum, even when free in solution, indicating that the presence of the salt bridge influenced the conformational exchange between different structural states (Fig. 6*A*). Together with the additional electron density observed for the CDR3 of mutant 20, this data showed that even in the absence of global structural changes, the mutations of VHH Z70 can modulate its conformational entropy, affecting ligand binding.

VHH thermal stability

To verify that the affinity optimization of the Z70-derived VHHs had not compromised stability, we measured their *in vitro* *T*ms. The *T*m was measured using a fluorescent reporter whose fluorescence increases once it binds the hydrophobic regions exposed during denaturation (Figs. S7 and S8). Z70 had a *T*m of 59.9 ± 0.9 °C that falls into the range reported for single-domain antibodies (34). Although there were few sequence differences between the individual VHH mutants, their thermal stability temperature range spanned about 15 °C. The G115E substitution in mutant 1 had little effect on VHH stability, with a loss of thermal stability of around 2 °C (Fig. 7). On the contrary, the P101S and S23C substitutions destabilized the VHHs, as shown by the low *T*ms of mutants 9, 15 (both carrying P101S, with denaturation temperature dropping by 10 °C) and of mutant 12 (carrying S23C, with denaturation temperature dropping by 7 °C). Although these mutations provided an increased affinity compared to Z70, the observed destabilization might contribute to a decrease efficiency in functional assays.

Self-aggregation of the VHH-mCherry constructs in HEK293 cells

We expect the VHH series derived from Z70 to present properties allowing their use in intracellular applications, similarly to the parent VHH. VHHs have already been shown to self-aggregate in cellular environments (35), and we showed that the purified mutated VHHs present a range of *in vitro* thermal stabilities that suggest their self-aggregation tendency in the intracellular compartment might also be affected (Fig. 6). We thus used HEK293 cells transfected with pmCherry constructs that produced VHH-mCherry to evaluate the aggregation of the Z70-derived VHH series expressed in the cellular environment. The presence of aggregates is noticed by the appearance of "puncta" inside the cells in contrast with a uniform fluorescence across the cell in the absence of aggregates as already described (35) (Fig. S9). Frequencies of self-aggregation of the various VHH-mCherry fusions were variable. The parent Z70 as well as mutant 1 (G115E), 3 (R47K), and 12 (S23C + G1115E) showed low-aggregation propensity, with puncta appearing in less than

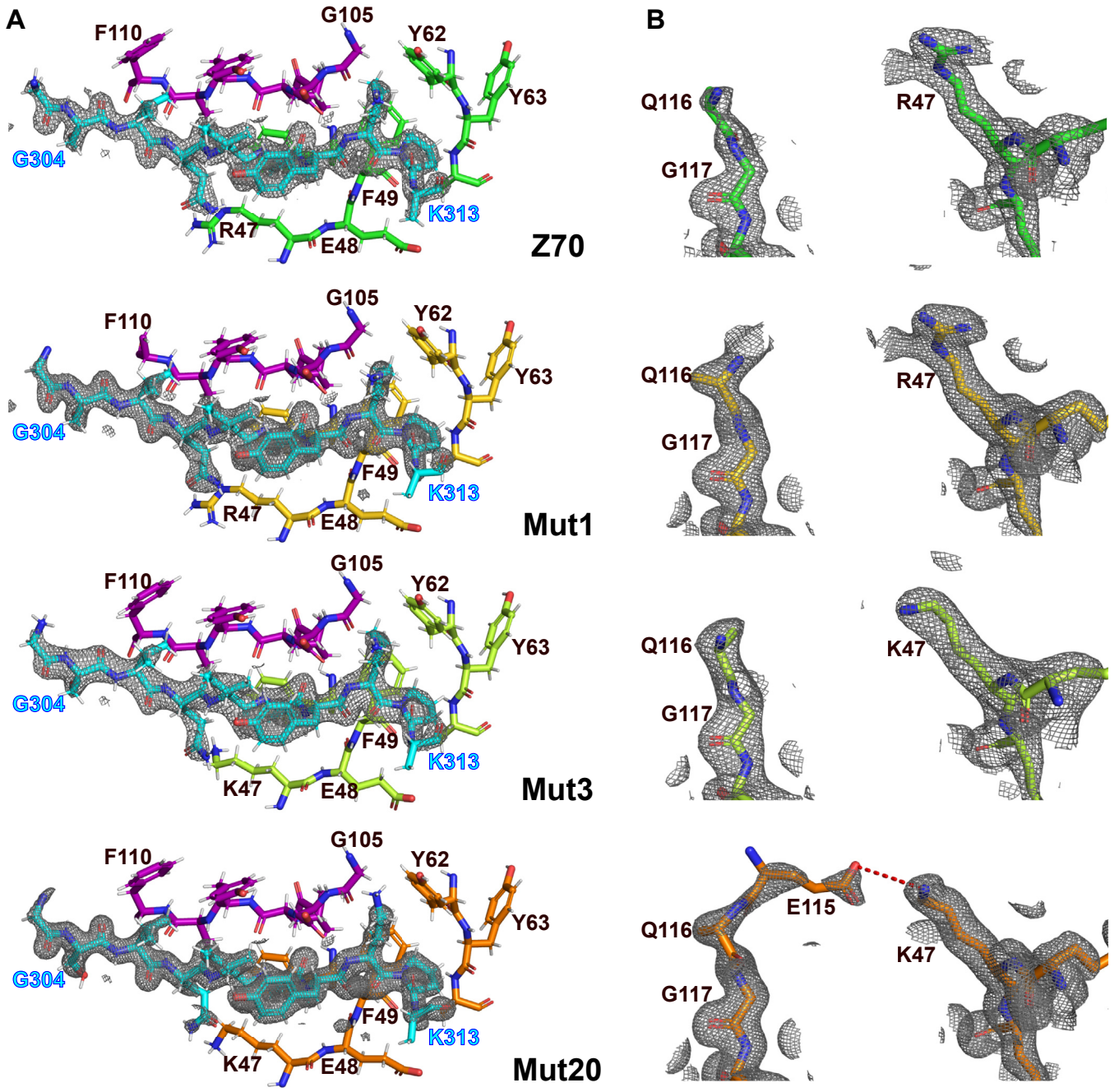

Figure 5. Comparison of Z70, mutant 1, 3, and 20 electron density maps. Z70, mutants 1, 3, and 20 are represented in *green, gold, pale green* and *orange*, respectively. Tau PHF6 peptide is colored *cyan*. *A*, environment of the peptide in all three structures remains unchanged. *B*, electron density (2fo-fc map contoured at 1 σ), shown as *mesh representation*, corresponding to the region surrounding residues 115 to 117 (*left*) and 46 to 48 (*right*) in VHH Z70 (*top*), mutant 1 (*middle*) and mutant 20 (*bottom*), respectively, showing the appearance of density for residue 115 from Z70 to mutant 20. A salt bridge is shown between K47 and E115 of mutant 20 in *red dashes*. VHH, variable heavy-chain of the heavy-chain–only antibody.

10% of the transfected cells (Fig. 8*A*). Other mutants showed higher aggregation propensity, such as mutants 5 (T96S), 9 (P101S + G115E), and 15 (R90G + P101S + G114E) with puncta in more than about half of the cells. This intracellular aggregation propensity is well correlated to the melting temperature (Pearson correlation coefficient of −0.87; Fig. 8*B*). Nevertheless mutants 5 and 12 that had similar melting temperatures (51.5–54 °C) showed different in-cell behaviors with high-aggregation propensity for mutant 5 (about 50% of cells with puncta) and low for mutant 12 (about 10% of cells with puncta).

Inhibition of in vitro *tau aggregation*

Z70 was primarily selected for its ability to inhibit tau aggregation both *in vitro* and *in vivo* (16). To determine how it affects tau aggregation at different molar ratios, we first studied Z70 effect on the tau-K18 fragment, which is a

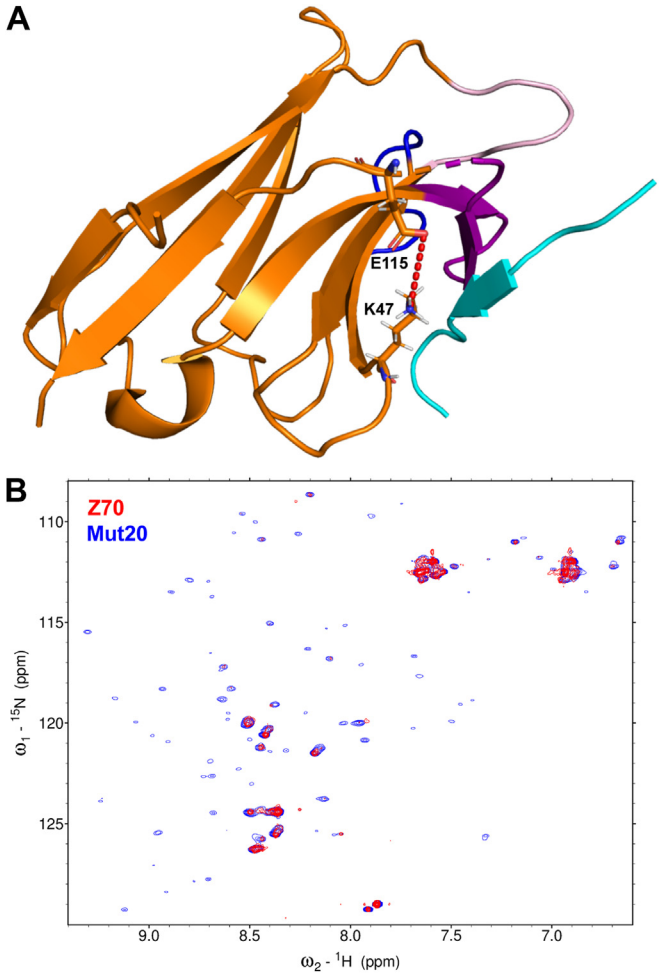

Figure 6. Conformational stabilization of mutant 20. *A, cartoon representation* of mutant 20 showing the salt bridge between residues K47 and E115 as *red dashes*. The framework region is colored *orange*, CDR 1 is represented in *pink*, CDR2 in *blue*, and CDR3 in *purple*, while the PHF6 peptide is colored *cyan*. *B*, superimposition of ^{1}H ^{15}N HSQC spectra of ^{15}N labeled mutant 20 in *blue* and VHH Z70 in *red* showing the detection of additional resonances in the spectrum of mutant 20 indicating a change in the conformational dynamics that could be favored by the K47-E115 salt bridge. CDR, complementarity-defining region; HSQC, heteronuclear single quantum coherence; VHH, variable heavy-chain of the heavy-chain–only antibody.

simplified model of choice for studying tau aggregation because it still contains the PHF6* and PHF6 aggregation-prone segments. Using the heparin-mediated assay in the presence of thioflavin as a fluorescent reporter of the aggregation, the results obtained (Fig. 9*A*) showed that with increasing VHH:tau-K18 M ratios, Z70 increasingly inhibited tau-K18 aggregation. This inhibition led to an increase in the aggregation lag phase as well as to a change in the slope of the aggregation curve, suggesting that Z70 affects multiple microscopic steps of the tau aggregation pathway (primary nucleation, elongation, and secondary nucleation (46)). The effect of Z70 is observed under substoichiometric conditions and is compatible with a model in which inhibition of tau aggregation by Z70 arises from interactions and shielding of the aggregation-prone PHF6 segment, consistent with its known role in the nucleation-polymerization process of tau amyloid formation (47, 48).

We next moved to validate these observations in full-length tau and to evaluate the efficiency of the different mutants to inhibit tau aggregation at subequimolar ratios in comparison with Z70 (Figs. S10 and S11). To facilitate comparison between the different VHHs, the data from the aggregation assays were analyzed as the thioflavin fluorescence intensity ratio between tau in the presence of a VHH and tau alone (positive control), for all points in the dynamic range of fluorescence corresponding to an intensity between 10 and 90% of the maximum fluorescence obtained for the positive control.

When using a VHH:tau stoichiometry of 0.5:1 (Fig. 9*B*), we have observed that mutants 1, 3, 12, 14, and 20 were more efficient than Z70, reducing the observed fluorescence intensity ratio to 12.7%, 17.3%, and 15.7% for mutants 1, 3, and 20, respectively, compared to 25% for Z70. In contrast, mutants 5 and 15 were less effective than Z70 and mutant 9 performed poorly (Fig. 9*B*), which was probably due to its tendency to self-aggregate in the conditions of the aggregation assay (Figs. S10 and S11). The use of a VHH:tau stoichiometry of 0.2:1 (Fig. S11) lead to some differences in these tendencies but confirmed mutants 1, 3, and 20 to be more efficient than Z70, with a reduction of the fluorescence intensity ratio to 40.5%, 25.4%, and 24.9%, respectively, compared to 46.2% for Z70 (Fig. S11). Mutant 5 performed better at the 0.2:1 VHH:tau stoichiometry than at the 0.5:1, probably because its propensity to self-aggregate is decreased at this lower concentration (Fig. S11).

Inhibition of tau seeding in HEK293 tau repeat domain P301S FRET biosensor reporter cells

We previously described the efficient inhibition of tau seeding by Z70 in a cellular model (16). As the various mutants had different inhibitory effects in the *in vitro* tau aggregation assay, we checked their efficiency in this cellular model as a comparison to and validation of the *in vitro* assay. The HEK293 seeding reporter cell line model constitutively expresses tau repeat domain (RD) (corresponding to tau microtubule-binding

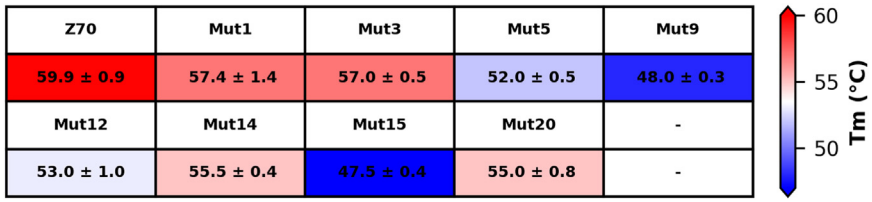

Figure 7. Thermal stabilities of the different VHHs in NMR buffer. VHH, variable heavy-chain of the heavy-chain–only antibody.

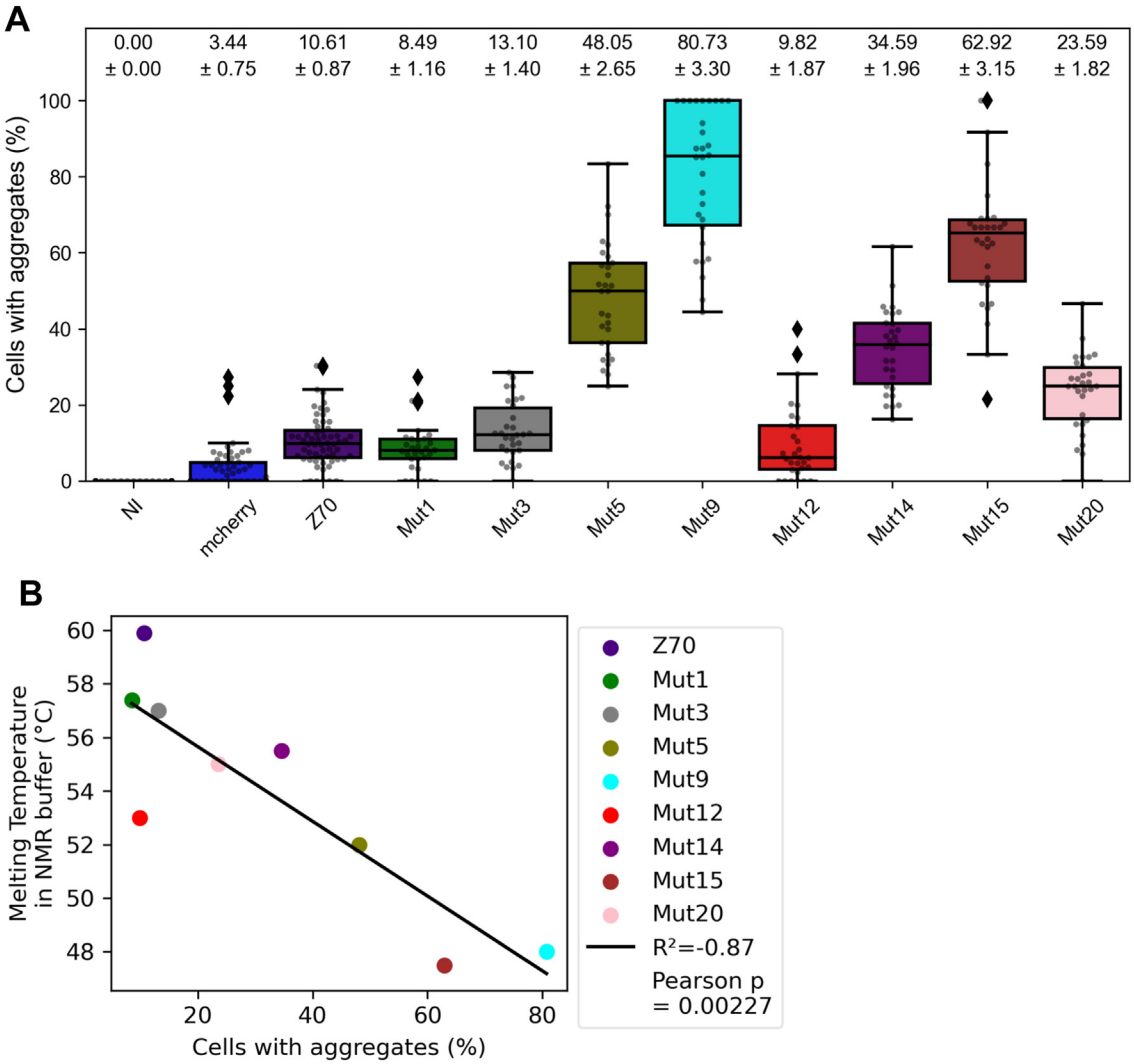

Figure 8. In-cell stabilities of the VHHs. *A*, percentage of mCherry-positive HEK293 cells showing aggregates (puncta) of VHH-mCherry 48 h after transfection. *B*, Pearson plot of the percentage of cells with aggregates in the self-aggregation assay *versus* melting temperatures in NMR buffer. VHH, variable heavy-chain of the heavy-chain–only antibody.

domain, MTBD or tau[244-372]), with a P301S mutation, fused to either cyan fluorescent protein or yellow fluorescent protein that together generate a FRET signal upon MTBD-P301S aggregation seeding (49). The intracellular aggregation of MTBD-P301S protein is induced by treating the cells with tau seeds (heparin-induced MTBD fibrils). VHHs were transfected 1 day prior to MTBD seed treatment. VHH F8-2 is used as negative control since its binding site is outside the MTBD as described previously (16, 20).

VHH F8-2 negative control was used as a 100% FRET-positive reference in the mCherry gated population for each individual experiment to minimize discrepancies arising from transfection efficiencies. Mutants 1, 3, and 12 retained at least Z70 level of efficiency (60.6 ± 1.7% of the reference) in this assay (Fig. 10) with 63.9 ± 1.9%, 62.8 ± 2.8%, and 59.4 ± 1.3%, respectively, with mutant 20 following closely (68.8 ± 3.7%). However, none of these mutants revealed significant difference when compared to Z70. Mutants 5 and 14 gave lower inhibition of seeding (82.3 ± 5.2% and 81.3 ± 3.4%), while mutants 9 and 15 failed to inhibit the seeding.

Selection of Z70 VHH variants based on complementary assays

We finally used the complementary *in vitro* and cellular assays to select Z70 VHH-derived mutants with a global view on their properties.

Interestingly, there is a correlation between the *in vitro* aggregation assay and the VHH inhibition capacity in the cellular seeding assay (Pearson correlation coefficient of 0.78; Fig. 11*A*) with mutant 9 being a clear outlier (Pearson correlation coefficient of 0.87 without mutant 9; Fig. 11*A*). The VHHs with lower performance in the *in vitro* assay performed poorly in the cellular assay (*e.g.,* mutant 15). The mutants 5, 9, and 15 poor *in vitro* inhibition efficiencies were revealed by low thermal stabilities, with low denaturation temperatures between 47.1 °C and 52.5 °C, coupled to poor stability in cells, with 45.4 to 84% of cells transfected with VHH-mCherry showing puncta. However, some VHHs retaining an inhibition efficiency close to parent Z70 in *in vitro* aggregation assays did not necessarily perform well in the cellular assays (*e.g.,* mutant 14). It is indeed striking that aggregation propensity of the

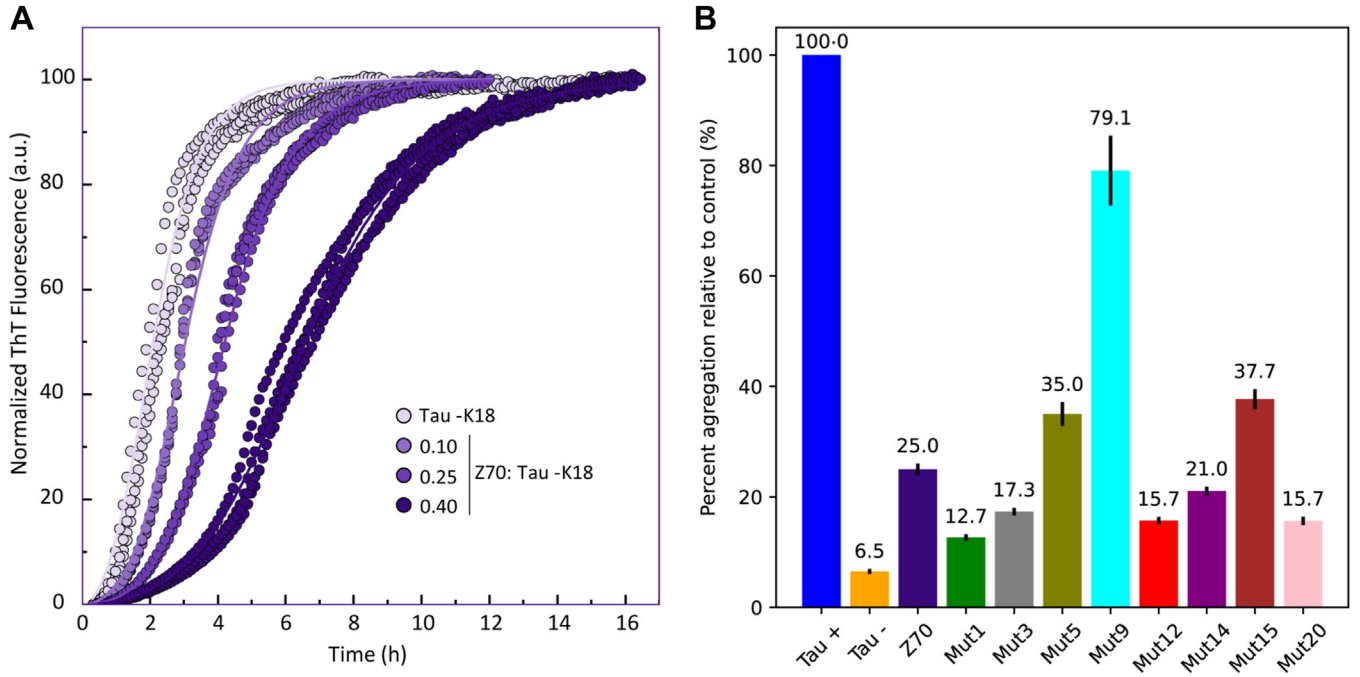

Figure 9. *In vitro* inhibition of tau aggregation by the VHHs. *A*, inhibition of tau-K18 aggregation by Z70 at VHH:Tau-K18 M ratios between 0.1 and 0.4 (n = 4) *B*, inhibition efficiency of different Z70-derived VHHs over tau aggregation tested at a molar ratio of 0.5:1 VHH:tau. Positive and negative controls correspond to tau in the presence of heparin (tau +) and the absence of heparin (tau –), respectively. The other conditions correspond to tau in the presence of heparin and the different VHHs at a VHH:tau ratio of 0.5:1. The percentage of aggregation corresponds to the fluorescence intensity ratio between tau in the presence of a VHH and tau alone (tau +) during the aggregation process. Data are represented as mean ± SEM, the mean value is written above the bars (n = 3). VHH, variable heavy-chain of the heavy-chain–only antibody.

VHH inside the cell is highly correlated to the inefficiency of the VHH to inhibit seeding in the reporter cells (Pearson correlation coefficient of 0.96; Fig. 11*B*). At the other end of the inhibition efficiency spectrum, parent Z70 as well as mutants 1, 3, and 12 showed low aggregation propensity in eukaryotic cells, with puncta appearing in less than 10% of the transfected cells (Fig. 8*A*) and were efficient inhibitors in the cellular seeding assays, the latter being consistent with their availability in the cytoplasm. Of note, mutant 12 despite its efficiency in these assays had a relatively low thermal stability (denaturation temperature 53 °C, Fig. 8*B*).

Discussion

Optimization of Z70 that binds a linear sequence within the intrinsically disordered tau protein led to the selection of eight mutants. All mutants were indeed optimized in their affinity toward the initial epitope, up to more than 6-fold. However, some mutants lost other essential properties in term of stability when produced in bacteria periplasm and purified and/or when expressed in eukaryotic cells. Yet, they were selected in the two-hybrid screen as better binders. Fusion to the GAL4-activation domain might help to stabilize these VHHs. However, our additional screen of in-cell stability is also done with

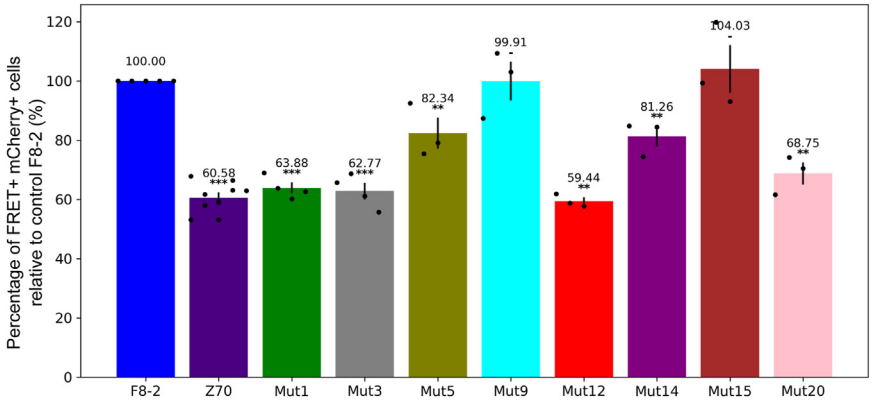

Figure 10. *In cellulo* inhibition of tau seeding by the VHHs. The percentage of FRET-positive cells, corresponding to cells with aggregated tau, is given for the mCherry-gated population, corresponding to transfected cells. Values are normalized relative to the experiment with F8-2 VHH-mCherry. Data are represented as mean ± SEM, the mean value is given above the bars and individual points are plotted. Statistical comparison between each VHH and F8-2 was carried out using post hoc Dunn's test after Kruskall–Wallis test with $p = 2.9*10^{-5}$, *** is $p < 0.001$, ** $p < 0.01$, and – is not significant. VHH, variable heavy-chain of the heavy-chain–only antibody.

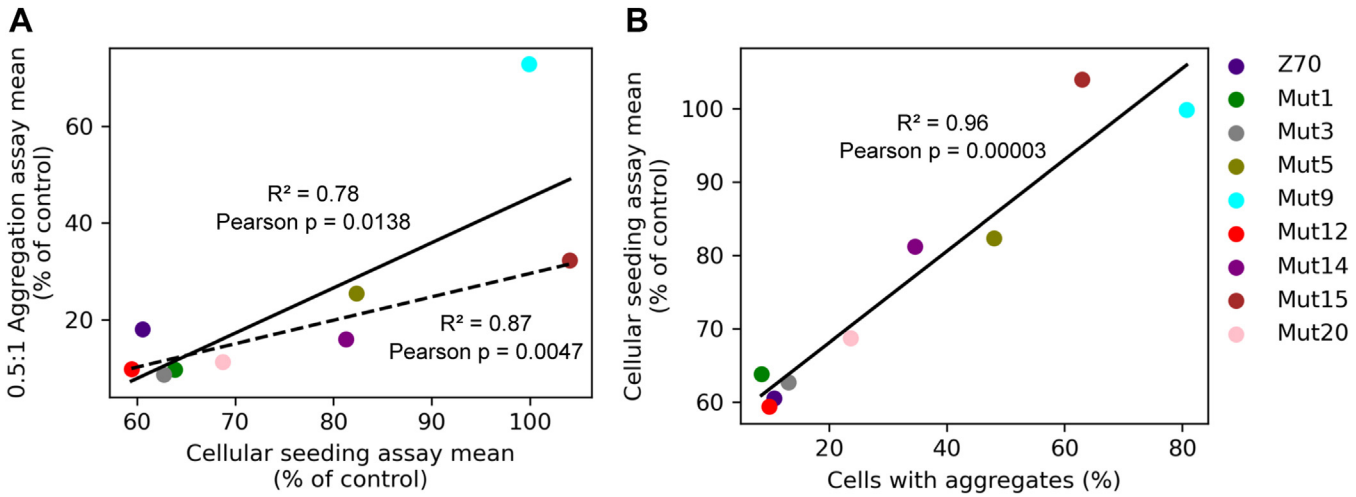

Figure 11. Pearson correlation plots. *A*, mean values of percentage of tau seeding in HEK293 tau repeat domain (RD) P301S FRET Biosensor seeding reporter cells (cellular seeding assay) *versus* mean values of *in vitro* aggregation assay with a ratio of 0.5 VHH for 1 tau. *Dashed line* is omitting the outlier mutant 9. *B*, mean values of percentage of tau seeding in HEK293 tau repeat domain (RD) P301S FRET biosensor seeding reporter cells (cellular seeding assay) *versus* percentage of cells showing punctate aggregates in HEK293 cells. VHH, variable heavy-chain of the heavy-chain–only antibody.

a fusion with the mCherry protein, which did not rescue the poor stability of some of the mutants, showing that this is an unlikely explanation. In the yeast two-hybrid assay in these screening conditions, the expression and the stability do not seem to be limiting points. This might not be the case in the seeding reporter cells, in which tau RD is expressed at high level and blocking the seeding thus requests optimal stability and binding properties of the VHHs.

The affinities that we have reached with the Z70 VHH series might still seem moderate considering the ability of some VHHs to bind to their target with sub nanomolar affinities (50, 51). However, VHHs are particularly efficient to bind cavities as epitopes (52), which is not the case when binding a linear tau epitope. Moreover, only a few VHHs directed against peptides are described, and in particular, one was developed as a capture and detection tool thanks to its high affinity defined by a Kd of 1.4 nM (53). Interestingly, similarly to the interaction of Z70 and the PHF6 peptide of tau, this peptide engages in the formation of an intermolecular β-sheet with the VHH recognition loop, which might underly the stability of the complex.

The two most common affinity enhancing substitutions (G115E and R47K) were never selected together in this initial screening leading us to generate such a mutant. Even though mutants 1 and 3 respective *in vitro* affinities were confirmed to be better than Z70, mutant 20 failed to give better affinity parameters as a combination of the two substitutions, suggesting that the mechanisms by which these substitutions enhance the affinity are not complementary. Atomic resolution structures of mutants 1, 3, and 20 combined with kinetics parameters of the interactions also suggest that their mechanisms of affinity enhancement might indeed differ. Mutant 1 with the introduction of a glutamic acid residue at position 115 had an improved k_{on} and very little structural or conformational dynamics differences with Z70, which argue for a charge effect facilitating the interaction with the basic tau protein (54, 55). The same effect might be achieved through the G115E mutation in mutants 9 and 12 and the G114E substitution in mutant 15 that all had an increased k_{on} compared to Z70, although to varying degrees.

Mutant 20 structural data suggest that the mutated residues G115E and R47K could form a salt bridge that would partially restrict the CDR3 flexibility as E115 is located at the loop basis and potentially decrease the entropic cost of the interaction. This hypothesis was supported by both NMR linewidths and X-ray electron density that showed a reduced conformational fluctuation for mutant 20, compared to VHH Z70 and the mutants 1 and 3. The ensuing stabilization of the complex is also supported by the lowest k_{off} of the VHH series for mutant 20. The link between a decrease flexibility of the CDR3 loop and a stronger antigen interaction is also demonstrated by the presence of an extra disulfide bond between the CDR3 and the CDR1 present in many VHHs (56). In contrast to mutants with the single unpaired G115E mutation, the double mutation R47K G115E in mutant 20 did not result in an improved k_{on} parameter compared to Z70. The double mutation in mutant 20 could suppress the G115E mutation benefit by neutralizing the positive charge at position 115 through the formation of the salt-bridge. Accordingly, the additional charges in mutant 1 might account for its excellent intracellular solubility (37), whereas its neutralization by the salt bridge could result in the poorer solubility in cells of mutant 20. The R47K substitution in mutant 3 also had an effect on the conformational dynamics, observed as the extended electronic density for the CDR3 and more resonances in the NMR spectra. However, these effects were more modest than for mutant 20, suggesting that additional mechanisms were involved to facilitate the binding.

Numerous factors are at play regarding the VHH stability, in a manner difficult to predict, currently preventing the opportunity to rationally design VHH stability. Any mutation of the VHHs could indeed affects their proper folding, *in vitro* (57) or

in cells (35), due to interference with other stabilizing interactions and/or due to improper positioning of the side chains. Accordingly, the stability of the Z70 variants were all decreased, although with varying degrees. Mutants 9 and 15 are the most affected with about a 10 °C *T*m decrease. We can hypothesize that the P301S mutation at the basis of the CDR3 loop might affect its optimal conformation that shields hydrophobic residues and/or increase the CDR3 conformational flexibility. The S23C destabilizing effect of mutant 12 is complex because this mutant VHH had a good intracellular solubility/stability despite the *T*m decrease. We propose that the S23C mutation hinders the proper formation of the C24-C99 FR1-FR3, stabilizing disulfide bridge *in vitro*, while in the cellular environment, the C23 could be reduced while the FR1-FR3 disulfide bridge could be formed after the folding process due to the optimal positioning of these two cysteine residues. It might explain the discrepancies for this specific mutant between the *in vitro* and in-cell data, compared to the other mutants. The T96S mutation was subtle but nevertheless affected the VHH stability. We can point that this position is almost universally conserved, arguing for its importance in the VHH proper folding.

To conclude on the mutation analysis, the charge effect provided by the G115E mutation had the greatest interest because it positively affected the affinity for the epitope without destabilizing the VHH or decreasing its intracellular solubility. Accordingly, this was the most abundant mutation found in the initial two-hybrid screen.

The correlation between the thermal stability of the VHHs and their in-cell stability was very good (Fig. 8*B*), with the noticeable exception of mutant 12 (S23C + G115E) that had a lower thermal stability than expected from all the other assays. We have found a very good correlation between the *in vitro* aggregation assay and the cellular seeding assay (Fig. 11), at the exception of mutant 9 (P101S + G115E). This can be easily rationalized based on the poor in-cell solubility and thermal stability of mutant 9. In a general manner, VHHs with poor intracellular solubility (mutant 5, 9, 14, 15, Figs. 8*A* and 11*B*) were found incapable of preventing intracellular tau seeding, while more soluble VHHs had better results (Figs. 10 and 11*B*), showing that the bioavailability of the VHHs in the intracellular compartment was a limiting factor. Our experiments thus agree with previous research suggesting that for single-chain antibodies scFv the intracellular efficiency is dictated by its intracellular stability rather than its *in vitro* affinity for its target (37).

We found that the *in vitro* experiments were reasonably predictive of the cellular assay outcomes and could serve as a first step of selection. Outliers in the correlations however argue that only the full set of complementary experiments can offer a comprehensive view of the VHHs properties. Among the different assays, the VHH self-aggregation assay in HEK293 cells provided the best correlation with other tests and particularly the cellular tau seeding assay, making it an excellent VHH assessment tool when targeting intracellular activity. Among the different optimized mutants, mutant 20 could be the best candidate as a recombinant tool for further use as a molecular probe with the large increase in its k_{off}, a parameter of choice for antibody selection. In contrast, mutants 1 (G115E) and 3 (R47K) showed the best behaviors in the different assays conducted here and could be good candidates as intracellular antibodies for further testing in *in vivo* experiments as improved versions of Z70. Overall, our experiment pipeline helped selecting the best mutant depending on their specific use, either as intracellular or recombinant VHH.

Experimental procedures

Optimization of VHH Z70 affinity

VHH Z70 was amplified from pHEN2 plasmid using Taq polymerase with 14 mM $MgCl_2$ and 0.2 mM $MnCl_2$ and a modified nucleotide pool (58). The amplified complementary deoxyribonucleic acids were transformed in yeast Y187 strain, together with a digested empty derivative of pGADGH vector (59), allowing recombination by gap repair in the vector. The VHH complementary deoxyribonucleic acids are expressed as preys, with a N-terminal Gal4-activation domain fusion (Gal4ADZ70). A library of 2.1 million clones was obtained, collected, and aliquoted. Tau variant 0N4R isoform (NM_016834.4) was expressed as bait with a C-terminal fusion with lexA (Tau-LexA) from pB29 vector, which is derived from the original pBTM116 (60). The library was screened at saturation, with 20 million tested diploids, using cell-to-cell mating protocol (61) by increasing the selection pressure with 100 mM 3AT. The improvement in affinity of some selected clones was confirmed by one-to-one mating assay with L40ΔGal4 (mata) yeast strain transformed with the bait, corresponding to tau variant 0N4R isoform with a C-terminal fusion with LexA (Tau-LexA) in pB29 plasmid, and Y187 (matα) yeast strain transformed with the prey, corresponding to a C-terminal Gal4-activation domain fusion (Z70-Gal4AD) (61). Diploids were grown on selection medium with increasing selection pressure by 3AT from 0 to 5 mM.

Production and purification of VHHs

Competent *Escherichia coli* BL21 (DE3) bacterial cells were transformed with the various PHEN2-VHH DNA constructs (13). For SPR immobilization on chips, crystallography assays, and ^{15}N labeled VHHs NMR experiments, the VHHs were produced using a pET22b plasmid featuring a recombinant sequence encoding a pelB leader sequence, a 6-His tag, a Tobacco Etch Virus protease cleavage site and the considered VHH with or without an additional C-terminal cysteine. Recombinant *E. coli* cells produced proteins targeted to the periplasm after induction by 1 mM IPTG in terrific broth medium or modified M9 medium containing minimal essential medium (MEM) vitamin mix 1× (Sigma-Aldrich), 4 g of glucose, 1 g of ^{15}N-NH_4Cl (Sigma-Aldrich), 0.5 g of ^{15}N-enriched Isogro (Sigma-Aldrich), and 0.1 mM $CaCl_2$ and 2 mM $MgSO_4$ for ^{15}N labeled VHHs. Production was pursued for 4 h at 28 °C or overnight at 16 °C before centrifugation to collect the cell pellet. Pellet was suspended in 200 mM Tris–HCl, 500 mM sucrose, 0.5 mM EDTA, pH 8 and incubated 30 min on ice. The resuspended pellet was then diluted four

times in water, yielding final concentrations of 50 mM Tris–HCl, 125 mM sucrose, 0.125 mM EDTA, pH 8, and complete protease inhibitor (Roche), and incubation was continued 30 min on ice. After centrifugation, the supernatant corresponding to the periplasmic extract was recovered. The VHHs were purified by immobilized-metal affinity chromatography (IMAC) (HisTrap HP, 1 ml, Cytiva), followed by size-exclusion chromatography (Hiload 16/60, Superdex 75, prep grade, Cytiva) in NMR buffer (50 mM sodium phosphate buffer [NaPi] pH 6.7, 30 mM NaCl, 2.5 mM EDTA, 1 mM DTT). For crystallography or SPR immobilization, VHHs were dialyzed against 50 mM Tris pH 8, 50 mM NaCl and cleaved with His-tagged Tobacco Etch Virus protease after a first IMAC step. Tobacco Etch Virus protease and cleaved 6-His tag were removed by a second IMAC step, the VHHs being recovered in the flow-through and concentrated to 400 to 500 μM for crystallography. Yield varies between the mutant VHHs, from around 1 mg (mutants 12, 15) up to 10 mg (mutant 20) per liter of bacterial fermentation.

VHH labeling and Western blotting

For Western blot experiments, 50 μM VHH with a terminal cysteine in NMR buffer were first buffer exchanged against PBS supplemented with 0.1 mM tris(2-carboxyethyl)phosphine using a Zeba spin desalting column. VHHs were labeled using 250 μM 5(6)-carboxytetramethylrhodamine C6 maleimide (Euromedex) for 4 h at 4 °C. The reaction was quenched using 1 mM DTT and probe leftover were removed by buffer exchange against PBS using a Zeba spin desalting column. Following SDS-PAGE, proteins were transferred from the polyacrylamide gel on a nitrocellulose membrane and blocked in PBS with 0.1% Tween 20 and 5% milk for 1 h. Labeled VHHs were used at a final concentration of 100 nM in PBS with 0.1% Tween 20 for 1 h incubation, followed by three washes in PBS with 0.1% Tween 20. Image acquisition was done using Amersham ImageQuant 800 (Cytiva).

Production and purification of labeled ^{15}N tau 2N4R and K18 tau fragment

pET15b-tau recombinant T7lac expression plasmid was transformed into competent *E. coli* BL21 (DE3) bacterial cells. A small-scale culture was grown in LB medium at 37 °C and was added at 1:10 V/V to 1 L of a modified M9 medium containing MEM vitamin mix 1× (Sigma-Aldrich), 4 g of glucose, 1 g of ^{15}N-NH_4Cl (Sigma-Aldrich), 0.5 g of ^{15}N-enriched Isogro (Sigma-Aldrich), 0.1 mM $CaCl_2$, and 2 mM $MgSO_4$. Recombinant ^{15}N tau (NCBI reference number NP_005901.2) production was induced with 0.5 mM IPTG when the culture reached an optical density at 600 nm of 0.8. Proteins were first purified by heating the bacterial extract, obtained in 50 mM NaPi pH 6.5, 2.5 mM EDTA, and supplemented with complete protease inhibitors cocktail (Sigma-Aldrich), 15 min at 75 °C. The resulting supernatant was next passed on a cation exchange chromatography column (Hitrap SP sepharose FF, 5 ml, Cytiva) with 50 mM NaPi pH 6.5 and eluted with a NaCl gradient. Tau proteins were buffer-exchanged against 50 mM ammonium bicarbonate (Hiload 16/60 desalting column, Cytiva) for lyophilization. Detailed procedure can be found in (62).

K18 expression and purification were performed according to (63).

NMR spectroscopy experiments

Analysis of the ^{15}N tau/VHH interactions were performed at 298 K on a Bruker Avance Neo 900 MHz spectrometer equipped with cryogenic probe. Trimethyl silyl propionate was used as internal reference. Lyophilized ^{15}N tau was diluted in NMR buffer with 10% D_2O and mixed with a VHH at 100 μM final concentration for each protein. Two hundred microliters of each mix in 3 mm tubes were sufficient to obtain the 2D ^{1}H, ^{15}N heteronuclear single quantum coherence (HSQC) spectra with 32 scans. ^{1}H, ^{15}N HSQC were acquired with 3072 and 416 points in the direct and indirect dimensions, for 12.6 and 25 ppm spectral windows, in the ^{1}H and ^{15}N dimensions, respectively.

Acquisitions of ^{15}N VHH spectra were performed at 298 K on a Bruker Avance Neo 900 MHz spectrometer equipped with cryogenic probe. Trimethyl silyl propionate was used as internal reference. ^{15}N VHHs were prepared in NMR buffer with 10% D_2O at 100 μM with and without PHF6 peptide at 200 μM final concentration. Two hundred microliters of each sample in 3 mm tubes were sufficient to obtain the 2D ^{1}H, ^{15}N HSQC spectra with 64 scans. ^{1}H, ^{15}N HSQC were acquired with 3072 and 256 points in the direct and indirect dimensions, for 12.8 and 28 ppm spectral windows, in the ^{1}H and ^{15}N dimensions, respectively.

Data were processed with Bruker Topspin 3.6 (https://www.bruker.com/en/products-and-solutions/mr/nmr-software/topspin.html) and analyzed with POKY (poky.clas.ucdenver.edu) (64). The spectra were rendered using POKY, and the intensity plots were designed with matplotlib (65).

SPR experiments

Affinity measurements were performed on a BIAcore T200 optical biosensor instrument (Cytiva). Recombinant tau proteins were biotinylated with 5 M excess of N-hydroxysuccimide-biotin conjugates (Thermo Fisher Scientific) during 4 h at 4 °C. Capture of biotinylated tau was performed on a SA sensor chip in 10 mM HEPES (4-(2-hydroxyethyl)-1-piperazineethanesulfonic acid), 150 mM NaCl, 3 mM EDTA and 0.5% v/v surfactant P20 (HBS-EP+ buffer, Cytiva). One flow cell was used as a reference to evaluate unspecific binding and provide background correction. Biotinylated-tau was injected onto a SA chip (Cytiva) at a flow-rate of 30 μl/min, until the total amount of captured tau reached 500 resonance units. VHHs were injected sequentially with increasing concentrations ranging between 0.125 and 2 μM in a single cycle, with regeneration (three successive washes of 1 M NaCl) between each VHH. Single-cycle kinetics analysis (66) was performed to determine association k_{on} and dissociation k_{off} rate constants by curve fitting of the sensorgrams using the 1:1 Langmuir model of interaction of the BIAevaluation software

2.0 (https://www.cytivalifesciences.com/en/us/support/software/biacore-downloads) (Cytiva). Dissociation equilibrium constants (K_d) were calculated as k_{off}/k_{on}.

VHH Z70 mutants' crystallization and structure determination

Z70 mutants 1, 3, and 20 concentrated to 400 to 500 μM were incubated with 1 mM of PHF6 peptide (PGGGSVQIVYKPKK) for 30 min prior crystallization screening. From an initial screening of around 600 conditions, optimal crystallization conditions were found to be 1.7 M ammonium sulfate, 4.25% (v/v) isopropanol, 30% (v/v) glycerol for mutants 1 and 3, or 0.095 M trisodium citrate pH 5.6, 19% (v/v) isopropanol, 19% (w/v) PEG 4000, and 5% (v/v) glycerol for mutant 20 (both conditions found in the Cryos Suite, Qiagen). Crystals were evaluated at SOLEIL synchrotron beamline PX1 and PX2A. All crystals belonged to space group $P6_522$ with cell parameters suggesting that the asymmetric unit contains one monomer (98% probability estimated from Matthews coefficient). The best diffraction was obtained at a resolution of 1.83 Å for mutant 1, 2.35 Å for mutant 3, and 1.54 Å for mutant 20. Structures were solved using molecular replacement (MOLREP (67)) with PDB 7qcq as template and refined to a R_{work} of 0.21, 0.2, and 0.17, and R_{free} of 0.24, 0.25, and 0.21 for mutants 1, 3, and 20, respectively, using REFMAC5 (68) and COOT (69). The structures were deposited in the PDB with access code 8opi, 8pii, and 8op0 for mutant 1, 3, and 20 respectively.

Thermal stability assay

Assays were carried out using a concentration of 80 μM VHH in NMR buffer and 10× SYPRO Orange (Invitrogen). Twenty microliters of each solution were placed in PCR multiwell plates and subjected to a temperature ramp from 25 °C to 94 °C set at 1 °C per 2 min in a MX3005P real-time PCR system (Agilent). Fluorescence is recorded every 2 min. Each test is carried out in triplicates. Thermal *T*m is defined as the maximal point of the derivative curve of the time evolution of the fluorescence intensity.

In-cell self-aggregation assay

HEK293 cells were seeded in 12-well plates (10^6 cells per well); 24 h later, cells were transfected with plasmids encoding mCherry, or the different VHH-mCherry constructs together with lipofectamine in optiMEM, as recommended by the manufacturer (Invitrogen). Forty-eight hours later, medium was removed, and cells were washed in prewarmed PBS before 30-min fixation at room temperature with 4% paraformaldehyde. After three successive washes in prewarmed PBS, the nuclei were stained with 4′,6-diamidino-2-phenylindole (1/10,000) for 15 min at room temperature. Cells were cover-slipped with VectaMount. Ten images per condition (n = 3 independent experiences) were acquired using a Zeiss AxioObserver Z1 (spinning disk Yokogawa CSU-X1, camera sCMOS Photometrics Prime 95B). The number of mCherry-positive cells containing puncta was quantified from three independent experiments, ten images per experiment, and per group. Data were plotted using matplotlib and seaborn (70).

In vitro *kinetic aggregation assays*

Tau-K18 aggregation kinetics were performed by recording the thioflavin-T (ThT) fluorescence intensity as a function of time in a plate reader (FLUOstar OPTIMA, BMGLabtech) with OPTIMA v2.20 (https://www.bmglabtech.com/en/microplate-reader-software/) equipped with a 440-nm excitation filter and a 480-nm emission filter. The fluorescence was recorded using bottom optics in half-area 96-well PEG-coated black polystyrene microplates with a clear bottom (Cat. 3881, Corning). The microplates were sealed with transparent foil to avoid evaporation. The aggregation assays were performed with 10 μM K18, 1 mM DTT (Cat. A1101, Applichem), 50 mM NaCl (Cat. MB15901, NZYTech), and 75 μM ThT (Cat. T3516, Sigma). K18 aggregation was induced by addition of 90 μg/ml (∼5 μM) of heparin (Cat. H3149, Sigma). In conditions with Z70, the used concentration ranged from 1 μM to 4 μM. Samples were prepared in 50 mM Tris–HCl, pH 7.4. The aggregation kinetics was performed at 37 °C in quiescent conditions. Four independent replicates were performed for each tested condition.

Tau 2N4R aggregation assays were performed with 10 μM tau and with increasing concentrations of VHHs (between 0 and 10 μM) in MES aggregation buffer containing 50 mM MES pH 6.9, 30 mM NaCl, 2.5 mM EDTA, 0.3 mM freshly prepared DTT, supplemented with 2.5 μM heparin H3 (Sigma-Aldrich) and 50 μM ThT (Sigma-Aldrich), at 37 °C. Experiments were reproduced three times in triplicates for each condition. The resulting fluorescence of ThT was recorded every 5 min/cycle within 200 cycles using PHERAstar microplate-reader (BMG labtech). The measures were normalized in fluorescence percentage, 100% being defined as the maximum value reached in the positive tau control, in each experiment. The bar plots are rendered with matplotlib.

Seeding assays in HEK293 reporter cell line

Stable HEK293 tau RD P301S FRET biosensor cells (American Type Culture Collection CRL-3275) were plated at a density of 100 k cells/well in 24-well plates. At 60% confluency, cells were first transiently transfected with the various pmCherry-N1 plasmid constructs allowing expression of the mCherry-fused VHHs. Transfection complexes were obtained by mixing 500 ng of plasmid diluted in 40 μl of opti-MEM medium, which included 18.5 μl (46.25% v/v) of opti-MEM medium with 1.5 μl (3.75% v/v) Lipofectamine 2000 (Invitrogen). Resulting liposomes were incubated at room temperature for 20 min before addition to the cells. Cells were incubated for 24 h with the liposomes and 1 ml/well of high glucose Dulbecco's modified Eagle's medium (American Type Culture Collection) with fetal bovine serum 1% (Life technologies). 8 μM of recombinant MTBD seeds were prepared *in vitro*, in the presence of 8 μM heparin, as described (49). Cells were then treated with MTBD seeds (10 nM/well) in the presence of transfection reagents forming liposomes as here above described.

FRET flow cytometry

Cells were recovered with trypsin 0.05% and fixed in 2% paraformaldehyde for 10 min, then suspended in PBS. Flow

cytometry was performed on an ARIA SORP BD (acquisition software (https://www.bdbiosciences.com/en-us/products/software/instrument-software/bd-facsdiva-software) FACS DIVA V7.0 BD, Biosciences). To measure cyan fluorescent protein emission fluorescence and FRET, cells were excited with a 405 nm laser. The fluorescence was captured with either a 466/40 or a 529/30 nm filter, respectively. To measure yellow fluorescent protein fluorescence, a 488 nm laser was used for excitation and emission fluorescence was captured with a 529/30 nm filter. mCherry fluorophore was excited with a 561 nm laser, and fluorescence was captured with a 610/20 nm filter. To selectively detect and quantify FRET, gating was used as described (49, 71). The FRET data were quantified using the KALUZA software (https://www.beckman.com/flow-cytometry/software/kaluza) analyze v2 and an in-house python script using FlowKit (72). Three independent experiments were done at least in triplicate, with at least 10,000 cells per analyzed replicate. Data were plotted using matplotlib and statistics computed with SciPy (73) using the nonparametric Kruskal–Wallis test, followed by Dunn's post hoc test against control VHH F8-2.

Data availability

Raw data are deposited in zenodo database (https://doi.org/10.5281/zenodo.8083246) or can be shared upon request. Three-dimensional crystallographic structure coordinates and electron densities are available for mutant 1 at https://www.rcsb.org/structure/8OPI, for mutant 3 at https://www.rcsb.org/structure/8OPII and mutant 20 at https://www.rcsb.org/structure/8OP0.

Supporting information—This article contains Supporting information.

Acknowledgments—We thank Dr Z. Lens for support on the T200 biacore measurements and P. Legrand for valuable support during data collection at beamline PX1 at the SOLEIL synchrotron facility (Paris, France). We acknowledge SOLEIL for the provision of synchrotron-radiation facilities. We also thank the BiCel platform from US 41 - UAR 2014 – PLBS for microscopy and FRET data acquisition. The NMR facilities were funded by the Nord Region Council, CNRS, Institut Pasteur de Lille, European Union, French Research Ministry, and Univ. Lille. Financial support from the IR INFRANALYTICS FR2054 CNRS for conducting the research is gratefully acknowledged.

Author contributions—J. M., S. B., M. C. S., L. E., and E. D. validation; J. M., O. Z., S. B., M. C. S., L. E., M. N., F.-X. C., C. D., and E. D. investigation; J. M., O. Z., M. C. S., X. H., J.-C. R., M. C., C. M. G., C. M. G., L. B., and C. D. writing-review and editing; X. H., J.-C. R., M. C., C. M. G., L. B., I. L., C. D., and E. D. methodology; X. H., M. C., C. M. G., L. B., I. L., C. D., and E. D. supervision; J.-C. R., C. M. G., L. B., I. L., C. D., and E. D. conceptualization; M. C. and E. D. formal analysis; M. C. and E. D. visualization; C. M. G., L. B., and I. L. project administration; C. M. G., L. B., and I. L. funding acquisition; I. L. and E. D. writing-original draft.

Funding and additional information—Our laboratories are also supported (L. B. and I. L.) by LiCEND (Lille Center of Excellence in Neurodegenerative Disorders). This study was supported (to L. B. and I. L.) by the LabEx (Laboratory of Excellence) DISTALZ (Development of Innovative Strategies for a Transdisciplinary approach to Alzheimer's disease ANR-11-LABX-01), by I-site ULNE (project TUNABLE) and by the ANR (project ToNIC, ANR-18-CE44-0016, project NanoTarget ANR-22-CE92–0061). Additional funding were obtained (to C. M. G.) by the Fundação para a Ciência e Tecnologia (Portugal) through PhD fellowship 2022.11023.BD (to M. C. S.) and BioISI center grants UIDB/04046/2020 (https://doi.org/10.54499/UIDB/04046/2020) and UIDP/MULTI/04046/2020 (https://doi.org/10.54499/UIDP/04046/2020). The study was partly funded by the European Union (TWIN2-PIPSA–Twinning for excel-lence in biophysics of protein interactions and self-assembly, GA 101079147, to C. M. G.). Our laboratories are supported (to C. M. G. and I. L.) by the Portugal-France bilateral exchange programme PESSOA –Campus France/Fundação para a Ciência e Tecnologia.

Conflict of interests—J.-C. R. is the CEO of Hybrigenic services. Part of the work is included in patent WO2020120644 NEW ANTI TAU SINGLE DOMAIN ANTIBODY L. I., B. L., D. E., D. C., R. J.-C., and A. A. The other authors declare that they have no conflicts of interest with the contents of this article.

Abbreviations—The abbreviations used are: 3AT, 3-amino-1,2,4-triazole; CDR, complementarity-defining region; FR, framework region; HSQC, heteronuclear single quantum coherence; IMAC, immobilized-metal affinity chromatography; MTBD, microtubule-binding domain; NaPi, sodium phosphate buffer; PDB, Protein Data Bank; PHF, paired helical filament; RD, repeat domain; SA, streptavidin; SPR, surface plasmon resonance; VHH, variable heavy-chain of the heavy-chain–only antibody.

References

1. Hamers-Casterman, C., Atarhouch, T., Muyldermans, S., Robinson, G., Hamers, C., Songa, E. B., *et al.* (1993) Naturally occurring antibodies devoid of light chains. *Nature* **363**, 446–448
2. Jovčevska, I., and Muyldermans, S. (2020) The therapeutic potential of nanobodies. *BioDrugs* **34**, 11–26
3. Pleiner, T., Bates, M., Trakhanov, S., Lee, C.-T., Schliep, J. E., Chug, H., *et al.* (2015) Nanobodies: site-specific labeling for super-resolution imaging, rapid epitope-mapping and native protein complex isolation. *eLife* **4**, e11349
4. Barakat, S., Berksoz, M., Zahedimaram, P., Piepoli, S., and Erman, B. (2022) Nanobodies as molecular imaging probes. *Free Radic. Biol. Med.* **182**, 260–275
5. Jiang, Y., Lin, Y., Krishnaswamy, S., Pan, R., Wu, Q., Sandusky-Beltran, L. A., *et al.* (2023) Single-domain antibody–based noninvasive *in vivo* imaging of α-synuclein or tau pathology. *Sci. Adv.* **9**, eadf3775
6. Peyvandi, F., Scully, M., Kremer Hovinga, J. A., Cataland, S., Knöbl, P., Wu, H., *et al.* (2016) Caplacizumab for acquired thrombotic thrombocytopenic purpura. *N. Engl. J. Med.* **374**, 511–522
7. Takeuchi, T., Kawanishi, M., Nakanishi, M., Yamasaki, H., and Tanaka, Y. (2022) Phase II/III results of a trial of anti–tumor necrosis factor multivalent NANOBODY compound ozoralizumab in patients with rheumatoid arthritis. *Arthritis Rheumatol.* **74**, 1776–1785
8. Ishiwatari-Ogata, C., Kyuuma, M., Ogata, H., Yamakawa, M., Iwata, K., Ochi, M., *et al.* (2022) Ozoralizumab, a humanized anti-TNFα NANOBODY® compound, exhibits efficacy not only at the onset of arthritis in a human TNF transgenic mouse but also during secondary failure of administration of an anti-TNFα IgG. *Front. Immunol.* **13**, 853008
9. Messer, A., and Butler, D. C. (2020) Optimizing intracellular antibodies (intrabodies/nanobodies) to treat neurodegenerative disorders. *Neurobiol. Dis.* **134**, 104619

10. Zheng, F., Pang, Y., Li, L., Pang, Y., Zhang, J., Wang, X., *et al.* (2022) Applications of nanobodies in brain diseases. *Front. Immunol.* **13**, 978513
11. Tsitokana, M. E., Lafon, P.-A., Prézeau, L., Pin, J.-P., and Rondard, P. (2023) Targeting the brain with single-domain antibodies: greater potential than stated so far? *Int. J. Mol. Sci.* **24**, 2632
12. Frenken, L. G. J., van der Linden, R. H. J., Hermans, P. W. J. J., Bos, J. W., Ruuls, R. C., de Geus, B., *et al.* (2000) Isolation of antigen specific Llama VHH antibody fragments and their high level secretion by Saccharomyces cerevisiae. *J. Biotechnol.* **78**, 11–21
13. Moutel, S., Bery, N., Bernard, V., Keller, L., Lemesre, E., de Marco, A., *et al.* (2016) NaLi-H1: a universal synthetic library of humanized nanobodies providing highly functional antibodies and intrabodies. *Elife* **5**, e16228
14. Desmyter, A., Spinelli, S., Roussel, A., and Cambillau, C. (2015) Camelid nanobodies: killing two birds with one stone. *Curr. Opin. Struct. Biol.* **32**, 1–8
15. Muyldermans, S. (2021) Applications of nanobodies. *Annu. Rev. Anim. Biosci.* **9**, 401–421
16. Danis, C., Dupré, E., Zejneli, O., Caillierez, R., Arrial, A., Bégard, S., *et al.* (2022) Inhibition of Tau seeding by targeting Tau nucleation core within neurons with a single domain antibody fragment. *Mol. Ther.* **30**, 1484–1499
17. Guilliams, T., El-Turk, F., Buell, A. K., O'Day, E. M., Aprile, F. A., Esbjörner, E. K., *et al.* (2013) Nanobodies raised against monomeric α-synuclein distinguish between fibrils at different maturation stages. *J. Mol. Biol.* **425**, 2397–2411
18. Lin, J., Figazzolo, C., Metrick, M. A., Sormanni, P., and Vendruscolo, M. (2021) Computational maturation of a single-domain antibody against Aβ42 aggregation. *Chem. Sci.* **12**, 13940–13948
19. Abskharon, R. N. N., Giachin, G., Wohlkonig, A., Soror, S. H., Pardon, E., Legname, G., *et al.* (2014) Probing the N-terminal β-sheet conversion in the crystal structure of the human prion protein bound to a nanobody. *J. Am. Chem. Soc.* **136**, 937–944
20. Dupré, E., Danis, C., Arrial, A., Hanoulle, X., Homa, M., Cantrelle, F.-X., *et al.* (2019) Single domain antibody fragments as new tools for the detection of neuronal tau protein in cells and in mice studies. *ACS Chem. Neurosci.* **10**, 3997–4006
21. Chan, P.-H., Pardon, E., Menzer, L., De Genst, E., Kumita, J. R., Christodoulou, J., *et al.* (2008) Engineering a camelid antibody fragment that binds to the active site of human lysozyme and inhibits its conversion into amyloid fibrils. *Biochemistry* **47**, 11041–11054
22. Abskharon, R., Pan, H., Sawaya, M. R., Seidler, P. M., Olivares, E. J., Chen, Y., *et al.* (2023) Structure-based design of nanobodies that inhibit seeding of Alzheimer's patient–extracted tau fibrils. *Proc. Natl. Acad. Sci.* **120**, e2300258120
23. Fichou, Y., Al-Hilaly, Y. K., Devred, F., Smet-Nocca, C., Tsvetkov, P. O., Verelst, J., *et al.* (2019) The elusive tau molecular structures: can we translate the recent breakthroughs into new targets for intervention? *Acta Neuropathol. Commun.* **7**, 31
24. Fitzpatrick, A. W. P., Falcon, B., He, S., Murzin, A. G., Murshudov, G., Garringer, H. J., *et al.* (2017) Cryo-EM structures of tau filaments from Alzheimer's disease. *Nature* **547**, 185–190
25. Scheres, S. H. W., Ryskeldi-Falcon, B., and Goedert, M. (2023) Molecular pathology of neurodegenerative diseases by cryo-EM of amyloids. *Nature* **621**, 701–710
26. Mudher, A., Colin, M., Dujardin, S., Medina, M., Dewachter, I., Alavi Naini, S. M., *et al.* (2017) What is the evidence that tau pathology spreads through prion-like propagation? *Acta Neuropathol. Commun.* **5**, 99
27. Goedert, M. (2020) Chapter Ten - tau proteinopathies and the prion concept. *Prog. Mol. Biol. Transl. Sci.* **175**, 239–259
28. Goedert, M., Clavaguera, F., and Tolnay, M. (2010) The propagation of prion-like protein inclusions in neurodegenerative diseases. *Trends Neurosci.* **33**, 317–325
29. Franzmeier, N., Neitzel, J., Rubinski, A., Smith, R., Strandberg, O., Ossenkoppele, R., *et al.* (2020) Functional brain architecture is associated with the rate of tau accumulation in Alzheimer's disease. *Nat. Commun.* **11**, 347
30. Franzmeier, N., Brendel, M., Beyer, L., Slemann, L., Kovacs, G. G., Arzberger, T., *et al.* (2022) Tau deposition patterns are associated with functional connectivity in primary tauopathies. *Nat. Commun.* **13**, 1362
31. Liu, Y., and Huang, H. (2018) Expression of single-domain antibody in different systems. *Appl. Microbiol. Biotechnol.* **102**, 539–551
32. Chao, S., Liu, Y., Ding, N., Lin, Y., Wang, Q., Tan, J., *et al.* (2022) Highly expressed soluble recombinant anti-GFP VHHs in Escherichia coli via optimized signal peptides, strains, and inducers. *Front. Mol. Biosci.* **9**, 848829
33. Sulea, T., Baardsnes, J., Stuible, M., Rohani, N., Tran, A., Parat, M., *et al.* (2022) Structure-based dual affinity optimization of a SARS-CoV-1/2 cross-reactive single-domain antibody. *PLoS One* **17**, e0266250
34. Goldman, E. R., Liu, J. L., Zabetakis, D., and Anderson, G. P. (2017) Enhancing stability of camelid and shark single domain antibodies: an overview. *Front. Immunol.* **8**, 865
35. Dingus, J. G., Tang, J. C. Y., Amamoto, R., Wallick, G. K., and Cepko, C. L. (2022) A general approach for stabilizing nanobodies for intracellular expression. *Elife* **11**, e68253
36. Wagner, T. R., and Rothbauer, U. (2021) Nanobodies – little helpers unravelling intracellular signaling. *Free Radic. Biol. Med.* **176**, 46–61
37. Kvam, E., Sierks, M. R., Shoemaker, C. B., and Messer, A. (2010) Physicochemical determinants of soluble intrabody expression in mammalian cell cytoplasm. *Protein Eng. Des. Sel.* **23**, 489–498
38. Fisher, A. C., and DeLisa, M. P. (2009) Efficient isolation of soluble intracellular single-chain antibodies using the twin-arginine translocation machinery. *J. Mol. Biol.* **385**, 299–311
39. da Silva, F. A., Santa-Marta, M., Freitas-Vieira, A., Mascarenhas, P., Barahona, I., Moniz-Pereira, J., *et al.* (2004) Camelized rabbit-derived VH single-domain intrabodies against vif strongly neutralize HIV-1 infectivity. *J. Mol. Biol.* **340**, 525–542
40. Martineau, P., Jones, P., and Winter, G. (1998) Expression of an antibody fragment at high levels in the bacterial cytoplasm. *J. Mol. Biol.* **280**, 117–127
41. Strube, R. W., and Chen, S.-Y. (2004) Enhanced intracellular stability of sFv–Fc fusion intrabodies. *Methods* **34**, 179–183
42. Shaki-Loewenstein, S., Zfania, R., Hyland, S., Wels, W. S., and Benhar, I. (2005) A universal strategy for stable intracellular antibodies. *J. Immunological Methods* **303**, 19–39
43. Danis, C., Dupré, E., Hanoulle, X., Landrieu, I., Lasorsa, A., Neves, J. F., *et al.* (2019) Nuclear magnetic resonance spectroscopy insights into tau structure in solution: impact of post-translational modifications. *Adv. Exp. Med. Biol.* **1184**, 35–45
44. Rennella, E., Sahtoe, D. D., Baker, D., and Kay, L. E. (2023) Exploiting conformational dynamics to modulate the function of designed proteins. *Proc. Natl. Acad. Sci. U. S. A.* **120**, e2303149120
45. Alderson, T. R., and Kay, L. E. (2021) NMR spectroscopy captures the essential role of dynamics in regulating biomolecular function. *Cell* **184**, 577–595
46. Shammas, S. L., Garcia, G. A., Kumar, S., Kjaergaard, M., Horrocks, M. H., Shivji, N., *et al.* (2015) A mechanistic model of tau amyloid aggregation based on direct observation of oligomers. *Nat. Commun.* **6**, 7025
47. von Bergen, M., Friedhoff, P., Biernat, J., Heberle, J., Mandelkow, E. M., and Mandelkow, E. (2000) Assembly of tau protein into Alzheimer paired helical filaments depends on a local sequence motif ((306)VQIVYK(311)) forming beta structure. *Proc. Natl. Acad. Sci. U. S. A.* **97**, 5129–5134
48. Lövestam, S., Li, D., Wagstaff, J. L., Kotecha, A., Kimanius, D., McLaughlin, S. H., *et al.* (2023) Disease-specific tau filaments assemble via polymorphic intermediates. *Nature* **625**, 119–125
49. Holmes, B. B., Furman, J. L., Mahan, T. E., Yamasaki, T. R., Mirbaha, H., Eades, W. C., *et al.* (2014) Proteopathic tau seeding predicts tauopathy *in vivo*. *Proc. Natl. Acad. Sci. U. S. A.* **111**, E4376–4385
50. Luginbühl, B., Kanyo, Z., Jones, R. M., Fletterick, R. J., Prusiner, S. B., Cohen, F. E., *et al.* (2006) Directed evolution of an anti-prion protein scFv fragment to an affinity of 1 pM and its structural interpretation. *J. Mol. Biol.* **363**, 75–97
51. Van Roy, M., Ververken, C., Beirnaert, E., Hoefman, S., Kolkman, J., Vierboom, M., *et al.* (2015) The preclinical pharmacology of the high affinity anti-IL-6R Nanobody® ALX-0061 supports its clinical development in rheumatoid arthritis. *Arthritis Res. Ther.* **17**, 135

52. Zavrtanik, U., Lukan, J., Loris, R., Lah, J., and Hadži, S. (2018) Structural basis of epitope recognition by heavy-chain camelid antibodies. *J. Mol. Biol.* **430**, 4369–4386
53. Braun, M. B., Traenkle, B., Koch, P. A., Emele, F., Weiss, F., Poetz, O., *et al.* (2016) Peptides in headlock – a novel high-affinity and versatile peptide-binding nanobody for proteomics and microscopy. *Sci. Rep.* **6**, 19211
54. Sheinerman, F. B., and Honig, B. (2002) On the role of electrostatic interactions in the design of protein-protein interfaces. *J. Mol. Biol.* **318**, 161–177
55. Selzer, T., Albeck, S., and Schreiber, G. (2000) Rational design of faster associating and tighter binding protein complexes. *Nat. Struct. Biol.* **7**, 537–541
56. Govaert, J., Pellis, M., Deschacht, N., Vincke, C., Conrath, K., Muyldermans, S., *et al.* (2012) Dual beneficial effect of interloop disulfide bond for single domain antibody fragments. *J. Biol. Chem.* **287**, 1970–1979
57. Kunz, P., Flock, T., Soler, N., Zaiss, M., Vincke, C., Sterckx, Y., *et al.* (2017) Exploiting sequence and stability information for directing nanobody stability engineering. *Biochim. Biophys. Acta Gen. Subj.* **1861**, 2196–2205
58. Cadwell, R. C., and Joyce, G. F. (1992) Randomization of genes by PCR mutagenesis. *PCR Methods Appl.* **2**, 28–33
59. Bartel, P. L., and Sternglanz, R. (1993) Cellular interactions in development: a practical approach. In: Hartley, D. A., ed. *Cellular Interactions in Development: A Practical Approach, illustrated Ed.*, Oxford University Press, Oxford, UK: 153–179. Practical approach series
60. Vojtek, A. B., and Hollenberg, S. M. (1995) Ras-Raf interaction: two-hybrid analysis. *Meth. Enzymol.* **255**, 331–342
61. Fromont-Racine, M., Rain, J. C., and Legrain, P. (1997) Toward a functional analysis of the yeast genome through exhaustive two-hybrid screens. *Nat. Genet.* **16**, 277–282
62. Danis, C., Despres, C., Bessa, L. M., Malki, I., Merzougui, H., Huvent, I., *et al.* (2016) Nuclear magnetic resonance spectroscopy for the identification of multiple phosphorylations of intrinsically disordered proteins. *J. Vis. Exp.* **118**, 55001
63. Moreira, G. G., Cantrelle, F.-X., Quezada, A., Carvalho, F. S., Cristóvão, J. S., Sengupta, U., *et al.* (2021) Dynamic interactions and Ca2+-binding modulate the holdase-type chaperone activity of S100B preventing tau aggregation and seeding. *Nat. Commun.* **12**, 6292
64. Lee, W., Rahimi, M., Lee, Y., and Chiu, A. (2021) POKY: a software suite for multidimensional NMR and 3D structure calculation of biomolecules. *Bioinformatics* **37**, 3041–3042
65. Hunter, J. D. (2007) Matplotlib: a 2D graphics environment. *Comput. Sci. Eng.* **9**, 90–95
66. Karlsson, R., Katsamba, P. S., Nordin, H., Pol, E., and Myszka, D. G. (2006) Analyzing a kinetic titration series using affinity biosensors. *Anal. Biochem.* **349**, 136–147
67. Vagin, A., and Teplyakov, A. (2010) Molecular replacement with MOLREP. *Acta Crystallogr. D Biol. Crystallogr.* **66**, 22–25
68. Murshudov, G. N., Skubák, P., Lebedev, A. A., Pannu, N. S., Steiner, R. A., Nicholls, R. A., *et al.* (2011) REFMAC5 for the refinement of macromolecular crystal structures. *Acta Crystallogr. D Biol. Crystallogr.* **67**, 355–367
69. Emsley, P., Lohkamp, B., Scott, W. G., and Cowtan, K. (2010) Features and development of coot. *Acta Crystallogr. D Biol. Crystallogr.* **66**, 486–501
70. Waskom, M. L. (2021) seaborn: statistical data visualization. *J. Open Source Softw.* **6**, 3021
71. Banning, C., Votteler, J., Hoffmann, D., Koppensteiner, H., Warmer, M., Reimer, R., *et al.* (2010) A flow cytometry-based FRET assay to identify and analyse protein-protein interactions in living cells. *PLoS One* **5**, e9344
72. White, S., Quinn, J., Enzor, J., Staats, J., Mosier, S. M., Almarode, J., *et al.* (2021) FlowKit: a Python toolkit for integrated manual and automated cytometry analysis workflows. *Front. Immunol.* **12**, 768541
73. Virtanen, P., Gommers, R., Oliphant, T. E., Haberland, M., Reddy, T., Cournapeau, D., *et al.* (2020) SciPy 1.0: fundamental algorithms for scientific computing in Python. *Nat. Methods* **17**, 261–272